Chapter 7. Remedial Ground Densification Techniques

7.1 Introduction

As stated in Chapter 2, the factor of safety against liquefaction (*FS*), as defined in this thesis, is the ratio of *Capacity* to *Demand*. To increase *FS*, the *Capacity* of the soil can be increased, the *Demand* imposed on the soil can be decreased, or both the *Capacity* and *Demand* can changed (increased or decreased) in such away that there is a net increase in their ratio. Several approaches for increasing *Capacity* and decreasing *Demand* are listed in Table 7-1.

Table 7-1. Approaches to increasing *Capacity* and decreasing *Demand*.

Capacity ↑	*Demand* ↓

C1) Increase Soil Density
 	
C2) Increase Effective Confining Pressure
 	
C3) Prevent Collapse of Soil Skeleton
    i)   Bond Soil Particles Together
    ii) Fill Voids with Grout
 	
C4) Provide Mechanism for Rapid
    Dissipation of Excess Pore Pressures
	D1) Soil Reinforcement/Seismic Shear
	    Stress Redistribution
	
	D2) Shift Fundamental Period of Soil
	    Profile

The general trends in the effects that these approaches have with respect to the stress-based liquefaction chart are illustrated conceptually in Figure 7-1. As shown in this figure, increasing the relative density of the soil or increasing the mean effective confining stress imposed on the soil (C1 and C2, respectively) results in an increase in penetration resistance, while the boundary separating the zones designated as "Liquefaction" and "No Liquefaction" is assumed to remain unchanged. This is contrary to preventing the collapse of the soil skeleton or providing a mechanism for the rapid dissipation of excess pore pressures (C3 and C4, respectively), for which the primary mode of improvement is a shift or modification of the boundary separating the zones designated as "Liquefaction" and "No Liquefaction" in such away that the "Liquefaction" zone is reduced. Also shown in Figure 7-1 is the reduction of the *Demand* by

redistribution of the earthquake-induced shear stress from the soil to the reinforcing elements (D1), or by shifting the fundamental period of the soil profile away from the predominant frequency of the earthquake motions (D2). However, the latter approach is rarely used in geotechnical earthquake engineering, and any consequential shifts in the fundamental period of soil profiles from ground improvements are typically ignored. The author could neither find studies examining the magnitude of shifts in the fundamental period of the profile resulting from remedial ground densification nor the significance of such shifts. Because earthquake motions are composed of a range frequencies of varying amplitudes, a consequential shift in the period of a profile due to soil treatment does not necessarily reduce the *Demand* imposed on the soil, but rather in some cases the *Demand* may increase.

A variety of soil improvement techniques has been developed to reduce the liquefaction susceptibility of soils, all of which rely on one or more of the mechanisms listed in Table 7-1. The grain-size ranges of soils most susceptible to liquefaction and potentially susceptible to liquefaction are shown in Figure 7-2. These boundaries were established from the results of sieve analyses performed on a number of soils that were known to have liquefied or not to have liquefied during past earthquakes (Tsuchida 1970). Superimposed on the grain-size distributions are the applicable grain-size ranges for various remediation techniques and the approaches on which they rely. With the possible exceptions of electrokinetic injection and precompression, all the techniques shown in Figure 7-2 can be used to reduce the liquefaction potential of soils. Mitchell and Gallagher (1998) provide general guidelines for selecting the appropriate remediation technique for a given set of field conditions.

Of particular interest to this research project are ground improvement techniques that, as a first step in the remediation process, induce controlled liquefaction, thus allowing the soil particles to rearrange into a denser packing as a result of additional vibration and upon dissipation of excess pore pressures. Vibro-compaction, deep dynamic compaction, and explosive compaction all fit into this category. All of these techniques improve the soil by increasing relative density (C1), while deep dynamic compaction and vibro-

compaction may also significantly increase the lateral effective confining pressure in the soil (C2).
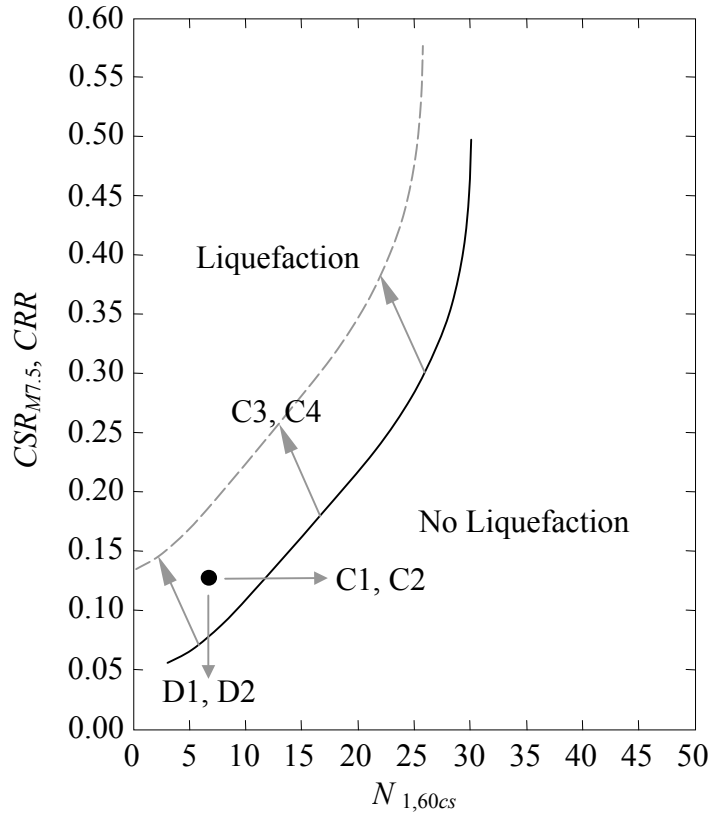

Figure 7-1. General trends of how the physical processes for reducing liquefaction susceptibility affect the stress-based liquefaction curve.

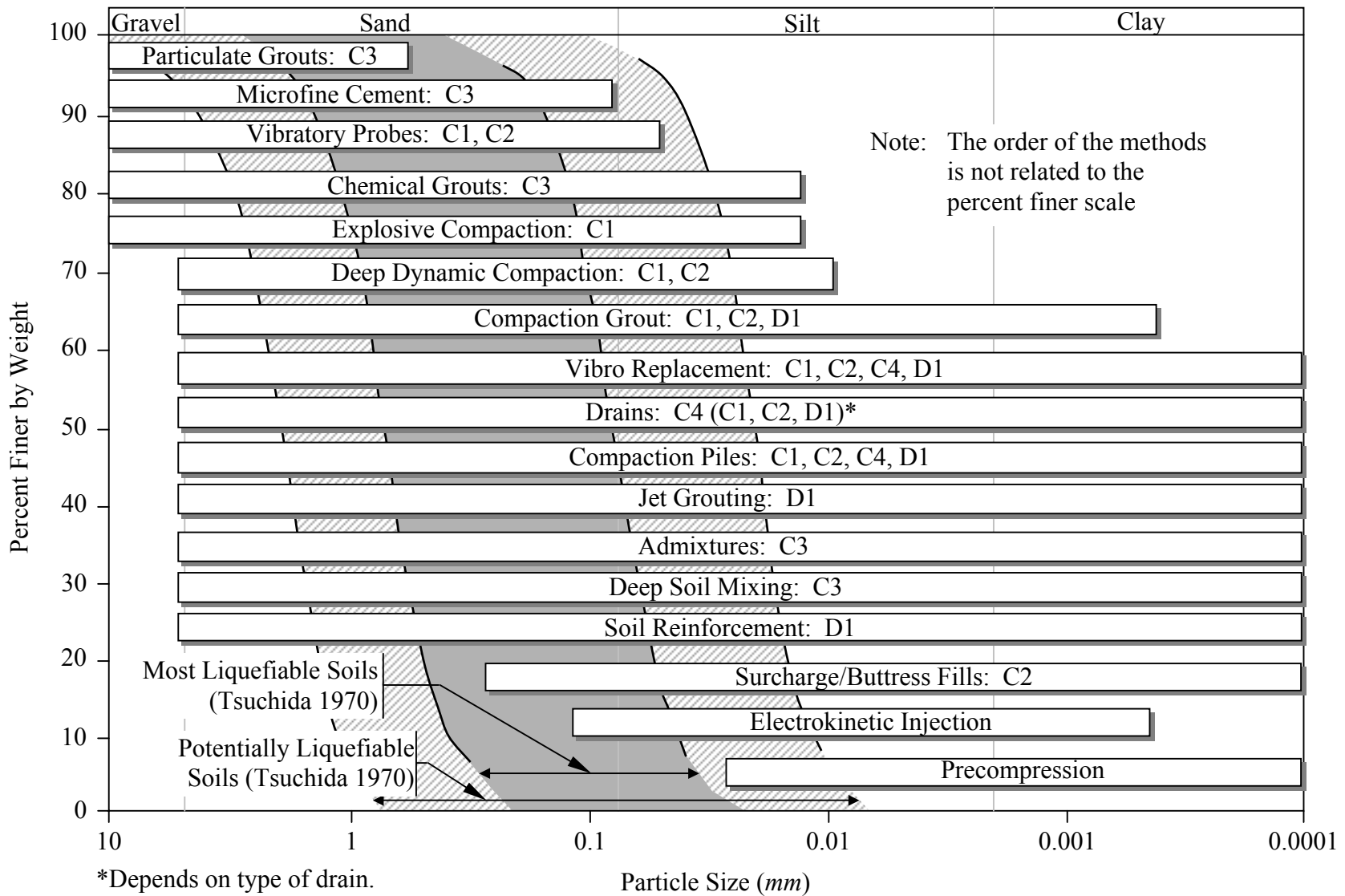This Page Was Intentionally Left Blank
to Ensure Proper Pagination

Figure 7-2. Applicable grain-size ranges for liquefiable soil improvement methods. (Adapted from Mitchell and Gallagher 1998).

The current empirical design procedures for implementing vibro-compaction, deep dynamic compaction, and explosive compaction are reviewed in the following sections of this chapter. Additionally, attention is given to the mechanisms contributing to the breakdown of the soil structure, which is requisite for liquefaction and thus a requisite for effective densification. Understanding these mechanisms is important to ensure the appropriateness of the numerical models used to represent the various densification techniques discussed in Chapter 8.

Finally, the empirical design procedures are used to compute the total energy required to densify a unit volume of soil by each of the densification techniques.

7.2 Vibro-Compaction

Vibro-compaction is a general term for densification techniques characterized by the insertion of long probes into the ground followed by compaction by vibration during withdrawal. The probes are typically hung from cranes or masts and are sunk to the desired treatment depth using vibratory methods, often supplemented by water jets at the tip (Mitchell 1981). The location of the vibrator on the probe, the directions of the induced vibrations (e.g., vertical, horizontal, torsional), and whether backfill is used distinguishes the various vibro-compaction techniques. In the case of vibrocompaction, the vibrator is incorporated inside the lower end of a torpedo shaped probe and induces torsional and horizontal vibrations (i.e., perpendicular to the long axis of the probe). On the contrary, the vibratory probe method uses heavy vibrators that are clamped to the upper end of long steel probes and induce vertical vibrations (i.e., parallel to the long axis of the probe). Cohesionless backfill is typically used in vibrocompaction; backfill is not commonly used in the vibratory probe method.

When applied to large areas, compaction points are typically arranged in either triangular or square grid patterns, as shown in Figure 7-3. The distance between the compaction points ranges from 1 to 3*m*, depending on the soil type, backfill type, probe type and energy, and the level of improvement required (Mitchell and Gallagher 1998). Ground

treatment depths of 20*m* can be routinely achieved by these methods, with depths in excess of 30*m* being reported (Mitchell 1981).

Triangular pattern — Tributary Area $= 0.87S^2$ — Compaction point

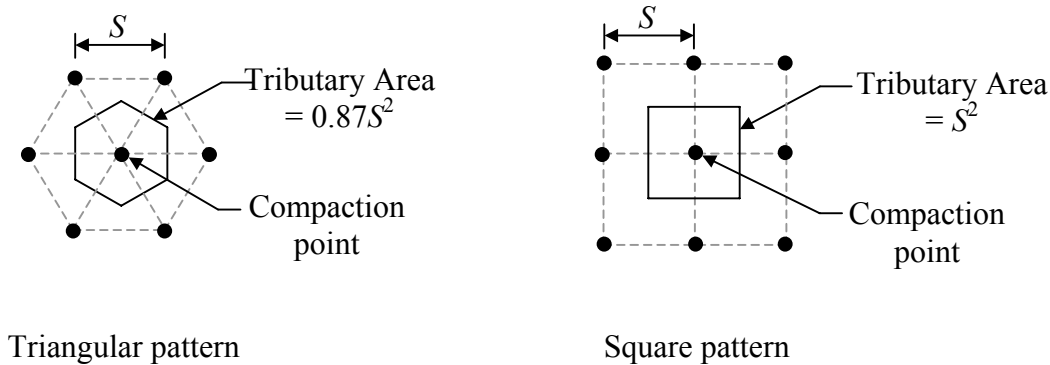Square pattern — Tributary Area $= S^2$ — Compaction point

Figure 7-3. Commonly used grid patterns for compaction points for implementing vibro-compaction techniques to large areas.

Several case studies have been published comparing the effectiveness of vibrocompaction versus the vibratory probe method (e.g., Brown and Glenn 1976; Saito 1977; Schroeder and Byington 1972; Neely and Leroy 1991). These studies draw conflicting conclusions as to which technique is more efficient. Probable reasons for this include different site conditions and the continued evolution of the techniques (e.g., more powerful vibrators and improved probe design). However, in general, vibratory probes require a smaller spacing between compaction points than vibrocompaction, but less operating time at each point to achieve a given level of improvement. Typical spacing for the vibratory probe method and vibrocompaction are 1 to 2*m* and 1.5 to 3*m*, respectively (Broms 1991). Additionally, because the vibratory probe method induces vibrations into the soil along the entire length of the probe, the top portion of the profile is treated for a longer duration than the bottom portion, which can result in non-uniform densification of the profile. On the contrary, targeted depths can treated as needed with vibrocompaction, resulting in more uniform densification of profiles.

Brief descriptions of vibrocompaction and the vibratory probe method are given in the following sections.

7.2.1 Vibrocompaction

Vibrocompaction was developed in Germany in 1934 by S. Steuermann and W.L. Degen, and its development continued there and in the United States where it was introduced in the 1940's (Degen and Hussin 2001). In past years, vibrocompaction was commonly referred to as vibroflotation. A photograph of an early vibrocompaction system is shown in Figure 7-4.

Figure 7-4. A 1937 photograph of an early vibrocompaction system or "Pfeilerruettler" (vibrating pile). (Photograph by W.L. Degen, courtesy of W.S. Degen, Vibro Systems Inc.).

Vibrocompaction is presently considered to be one of the premier methods for densifying deep sand deposits. The required equipment for implementing this technique consists of three main parts: the vibrator, extension tubes, and a supporting crane. The combined vibrator and extension tubes are referred to as the vibroflot. A schematic diagram of the equipment and process is given in Figure 7-5. As depicted in this figure, the vibroflot is usually jetted into the ground to the desired depth of improvement. The soil densifies during withdrawal of the vibroflot as a result of lateral and torsional vibrations while the

vibroflot is repeatedly inserted and withdrawn in about 1*m* increments. The cavity that forms at the surface is backfilled with sand or gravel to form a column of densified soil (Mitchell and Gallagher 1998). The anatomy of a densified zone is further illustrated in Figure 7-6.
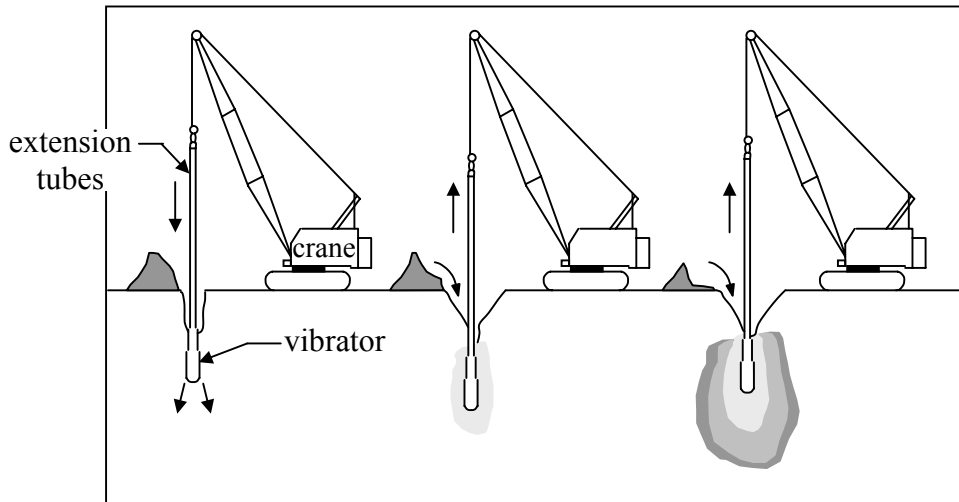

Figure 7-5. Schematic diagram of the equipment and process of soil densification using vibrocompaction technique. (Adapted from Hayward Baker 1996).

Extension
Tube

Vibroflot

Vibrator

A. Cylinder of compacted material
added from the surface to compensate
for the loss of volume caused by the
increase of density of the compacted
soil.

B. Cylinder of compacted material
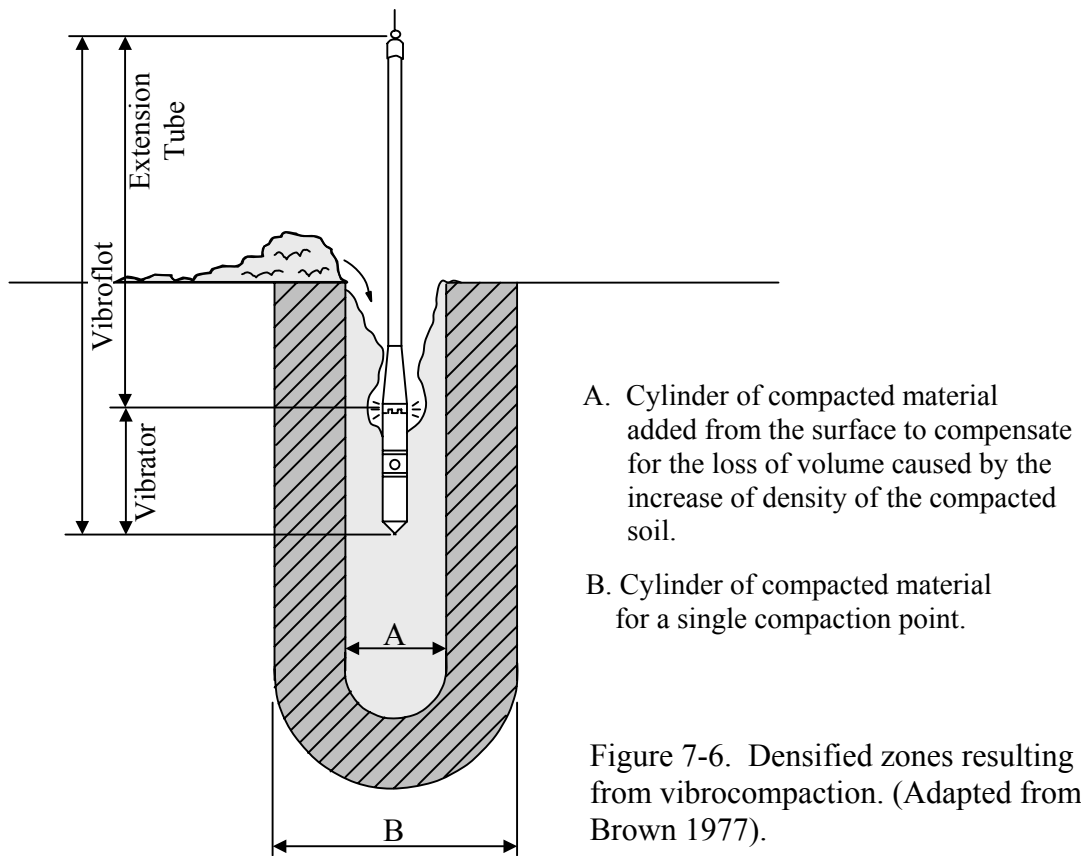for a single compaction point.

A

B

Figure 7-6. Densified zones resulting
from vibrocompaction. (Adapted from
Brown 1977).

Although more powerful motors are continually being used in the vibrator, the physical

size of the motor is limited by the size of the probe. In turn, the size of the probe is

limited by its ability to penetrate into the soil; a typical probe diameter is about $0.4m$.

Two commonly used probes are shown in Figure 7-7. In addition to the probes shown in

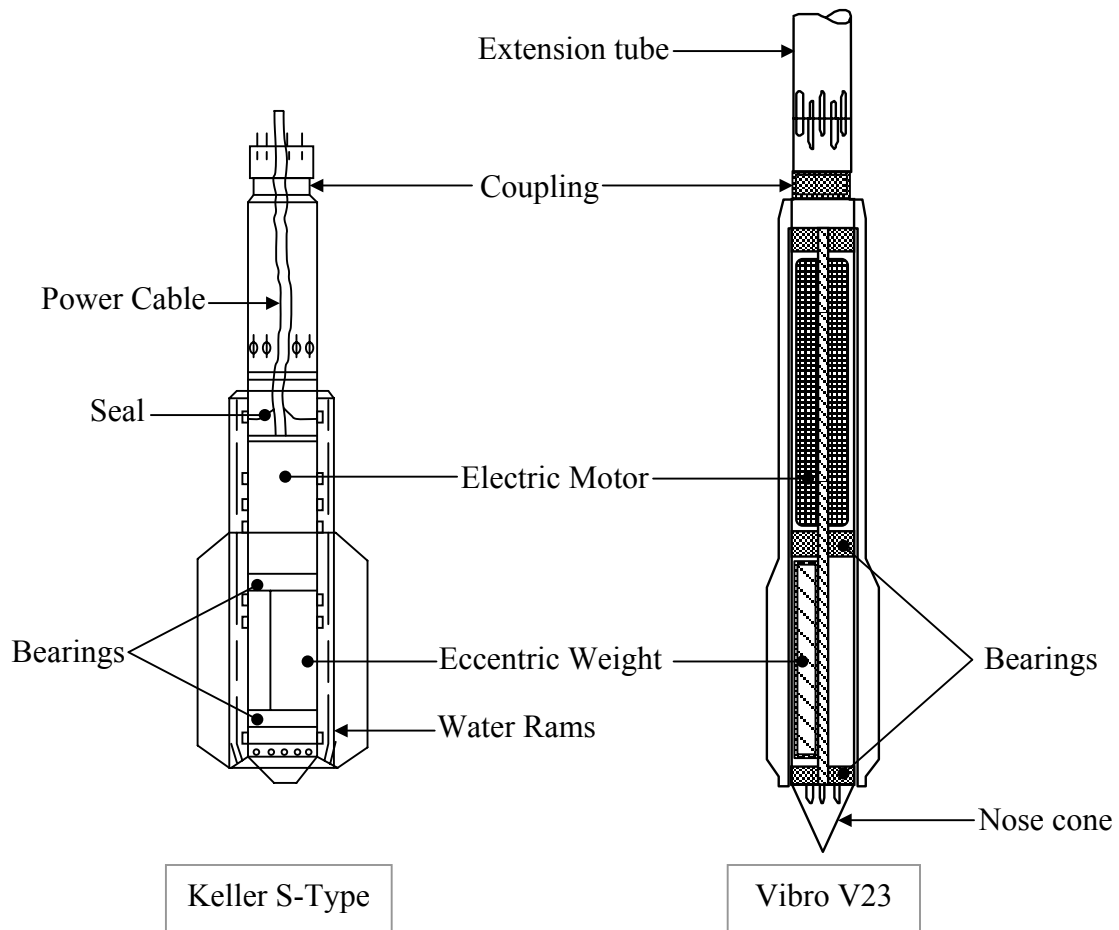this figure, Table 7-2 lists the specifications of several other commonly used probes.

Figure 7-7. Common vibrators used in vibrocompaction. The relative sizes of the vibrators are not to scale. (Adapted from Hayward Baker 1996 and Degen and Hussin 2001).

Table 7-2. Specifications of commonly used vibrators. (From Degen and Hussin 2001).

Manufacturer	Bauer	Bauer	Keller	Keller	Keller	Keller	Vibro	Vibro
Machine name	TR13	TR85	M	S	A	L	V23	V32
Length (m)	3.13	4.20	3.30	3.00	4.35	3.10	3.57	3.57
Diameter (m)	300	420	290	400	290	320	350	350
Weight (kg)	1000	2090	1600	2450	1900	1815	2200	2200
Motor (kW)	105	210	50	120	50	100	130	130
rpm	3250	1800	3000	1800	2000	3600	1800	1800
Displ. Amp. (mm)	6	22	7.2	18	13.8	5.3	23	32
Dynamic Force (kN)	150	330	150	280	160	201	300	450

The rotation of the eccentric mass induces a conical movement of the vibroflot about the coupling connecting the vibrator and the extension tubes, as shown in Figure 7-8. The displacement amplitudes listed in Table 7-2 correspond to those measured while the vibrator is suspended in air and will be much less when penetrated in the soil.
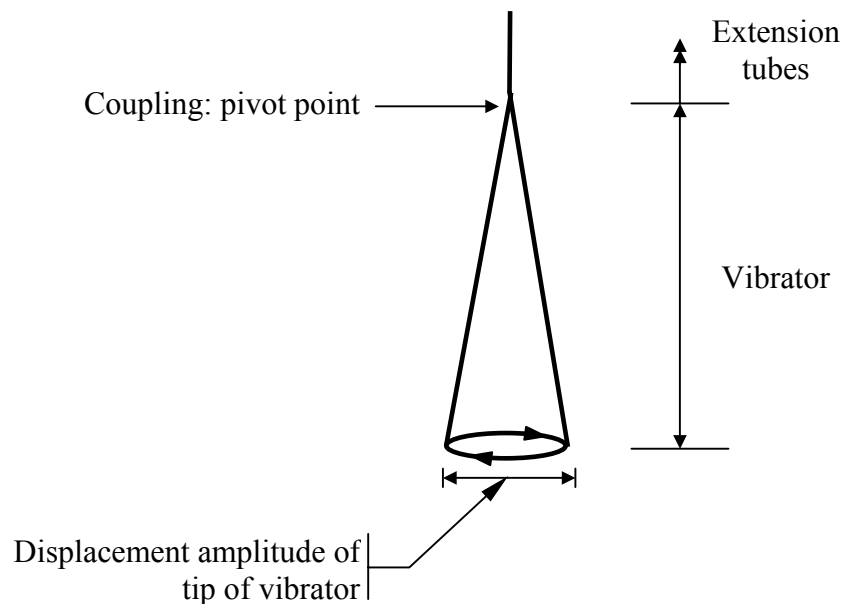

Figure 7-8. Conical movement of vibrator unit.

The interaction of the vibroflot and the surrounding soil is very complex, especially when water and backfill are introduced into the borehole during vibration. A conceptual illustration of the interaction and the induced stresses and strains on the surrounding soil is shown in Figure 7-9. As may be seen in this figure, the horizontal impacting force causes both a radial strain (ε_{rr}) and lateral strain ($\varepsilon_{\theta\theta}$) in the soil, resulting in a deviatoric shear strain (γ_{dev}) as given by the following expression.

$$\gamma_{dev} = \frac{1}{2} \cdot \left[\varepsilon_{rr} - \varepsilon_{\theta\theta} \right] \tag{7-1}$$

where: γ_{dev} = Deviatoric shear strain.

$\varepsilon_{\theta\theta}$ = Lateral strain.

ε_{rr} = Radial strain.

Furthermore, the torsional motion of the vibroflot induces a shear stress (τ) in the soil. Both the deviatoric shear strain and torsional shear stress contribute the breakdown of the soil structure, facilitated by the influx of water that reduces the effective confining stresses imposed on the soil. A thorough treatment of the vibroflot-soil interaction is given in Fellin (2000), as related to the author by Degen (2001).

When vibrocompaction is used to densify large areas, compaction points are usually arranged in triangular or square grid patterns as shown in Figure 7-3. The approximate variation of the post-treated relative density as a function of the tributary area per compaction point and soil type is shown in Figure 7-10. Although this figure may be used to select the initial spacing of the compaction points, field tests should be performed to finalize the design.
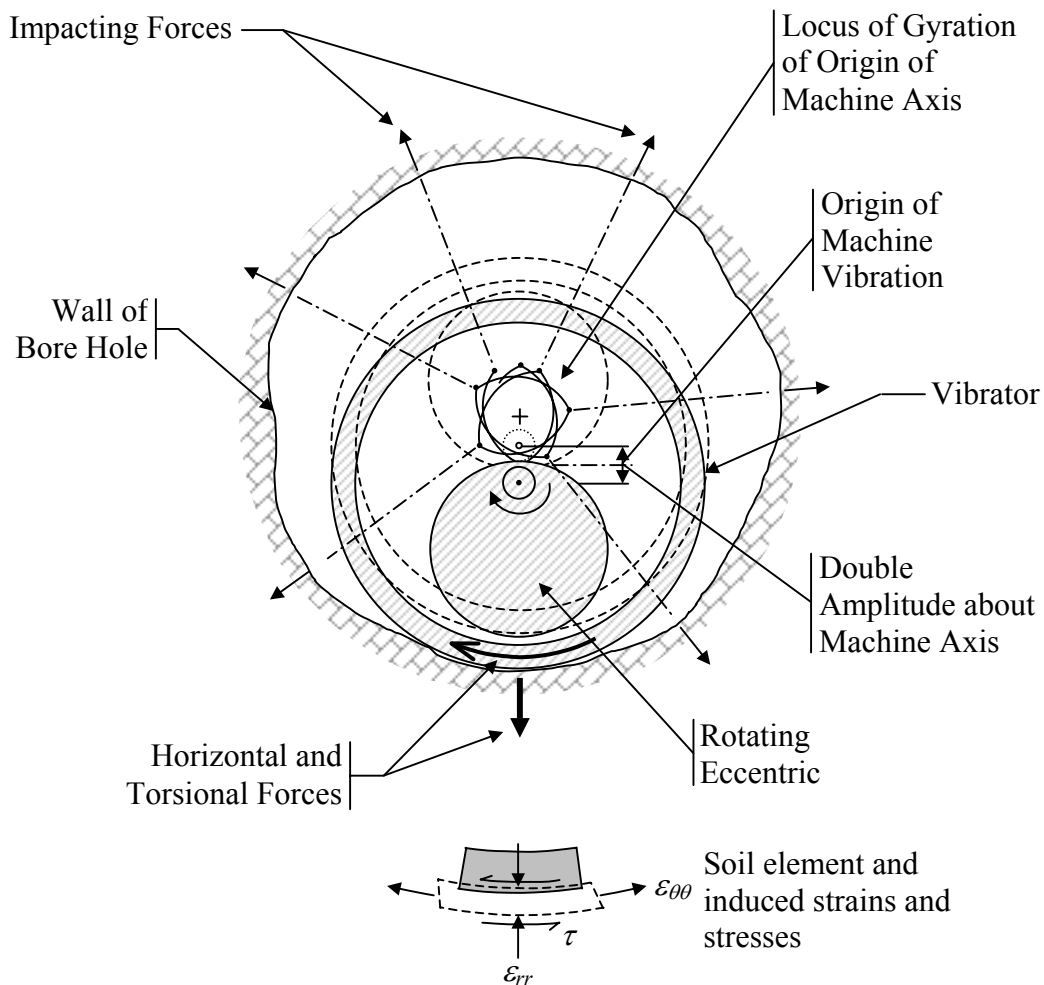
Figure 7-9. Illustration of the horizontal impacting forces and torsional shear induced by the vibroflot. (Adapted from Greenwood 1991).

As a side note, the specifics behind the development of Figure 7-10 could not be found by the author. However, it is surmised that the vertical axis is actually "equivalent relative density" and not the true relative density of the post-treated soil. The post-treated soil will have significantly higher lateral effective confining stresses than natural soil deposits. As a result, relative densities estimated from penetration resistances using standard correlations may be over estimated and are referred to as "equivalent relative densities" (Mitchell 1981). The use of standard correlations between D_r and SPT N-values in developing Figure 7-10, as opposed to direct measurement of D_r, was alluded to in Baez (1995). Because current liquefaction procedures correlate liquefaction potential

directly with penetration resistance, and not relative density as was done in the past, the use of equivalent relative densities is no longer necessary. Accordingly, Figure 7-10 was updated by including penetration resistance on the right vertical scale, as well as the equivalent relative density scale.
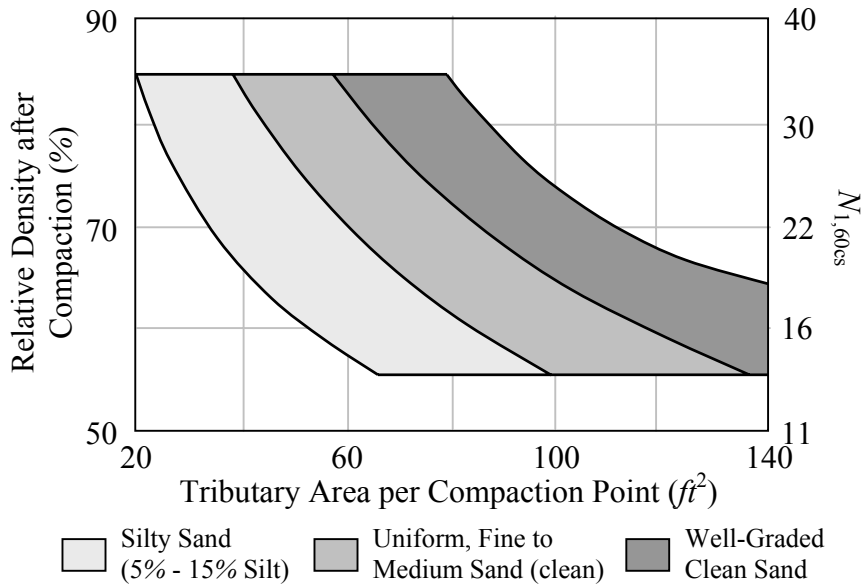

Figure 7-10. Approximate variation of post-compaction relative density and tributary area per compaction point. (Adapted from Dobson and Slocombe 1982).

It should be noted that a closer grid spacing does not always lead to increased penetration resistance at the center of the compaction points, and the appropriate grid spacing will likely vary as a function of the type of probe used (Degen and Hussin 2001). The variation of post-treated CPT tip resistance is shown as a function of distance from a compaction point in Figure 7-11. For the particular project illustrated in this figure, a minimum tip resistance of $15 MPa$ was specified for all locations. For a probe spacing of $3.7m$, the minimum tip resistance could not be achieved at the center of the compaction points using the V23 probe, but could be achieved using the V32 probe. However, at other locations higher tip resistances were measured in the soil densified with the V23 probe. For this particular project, adherence to the specified guidelines of a minimum tip

resistance of $15MPa$ at all locations (i.e., densification of the soil using the V32), may not have resulted in the best overall improvement of the site.
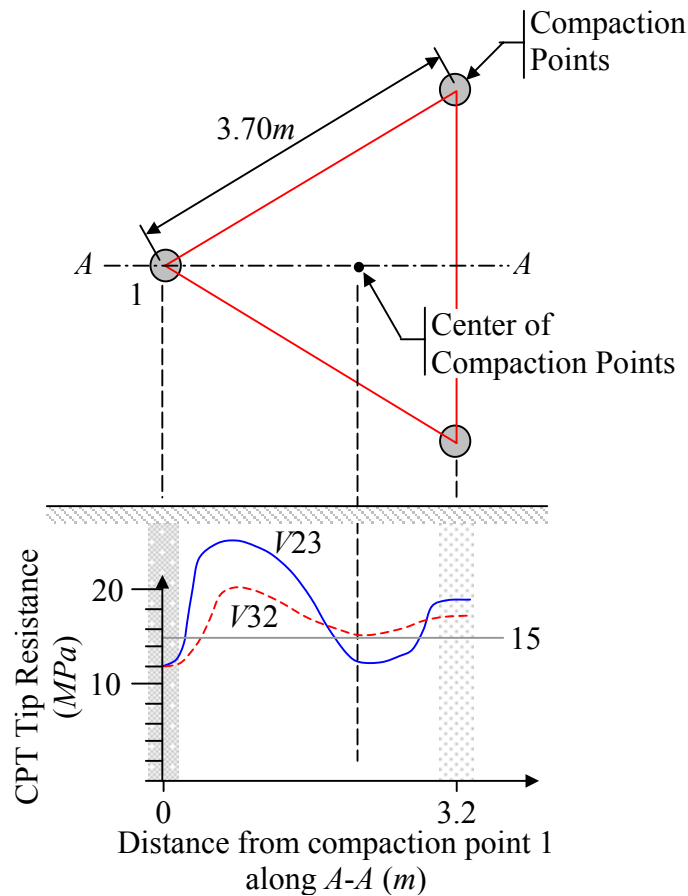

Figure 7-11. Variation of post-treated CPT tip resistance with distance from compaction point for two different vibrators. (Adapted from Degen and Hussin 2001).

7.2.2 The Vibratory Probe Method

The vibratory probe method uses heavy vibrators attached to the top of a long probe suspended from a crane or mast. The vibrator excites the probe in the vertical direction (i.e., parallel to the long axis of the probe), as is shown in Figure 7-12. Because the vibrator is mounted on the top of the probe and does not penetrate the soil, it is not limited in physical size. As with vibrocompaction, the probe is rapidly inserted to the desired depth of improvement, and the compaction occurs during the extraction of the probe. Water jetting may be used but is not normally required, which makes the method

simple to implement. Backfilling the cavity created by compaction of the soil deposit is optional. Repeated extraction and insertion of the probe in increments is common.
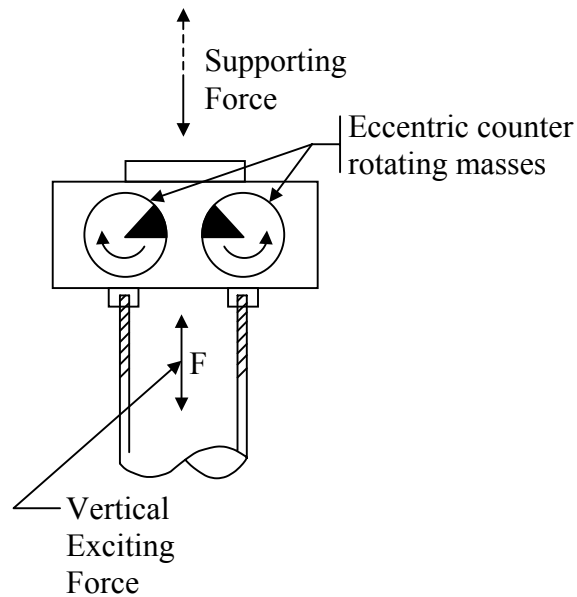

Figure 7-12. Conceptual illustration of the orientation of the exciting force of the vibratory probe. (Adapted from Greenwood 1991).

Two shortcomings of the vibratory probe method are lack of uniformity of the improved ground and depth limitations. Because the vibratory probe induces vibrations in the soil surrounding the probe for its entire depth of penetration, soil near the top of the profile is vibrated for a longer duration than soils at depth. This may lead to non-uniform densification with depth in the profile. Additionally, due to the flexibility of the probes, the amplitude of the induced vibration decreases along the length of the probe, which limits the maximum depth at which soil can be treated.

A conceptualization of the vibratory probe-soil interaction is shown in Figure 7-13. As shown in this figure, Rayleigh, P- , and S-waves are generated resulting in a complex shearing of the soil. As a further complexity, axial bending of the probe likely occurs (e.g., the probe becomes S-shaped), thus inducing compression waves in the soil at various locations along the length of the probe.
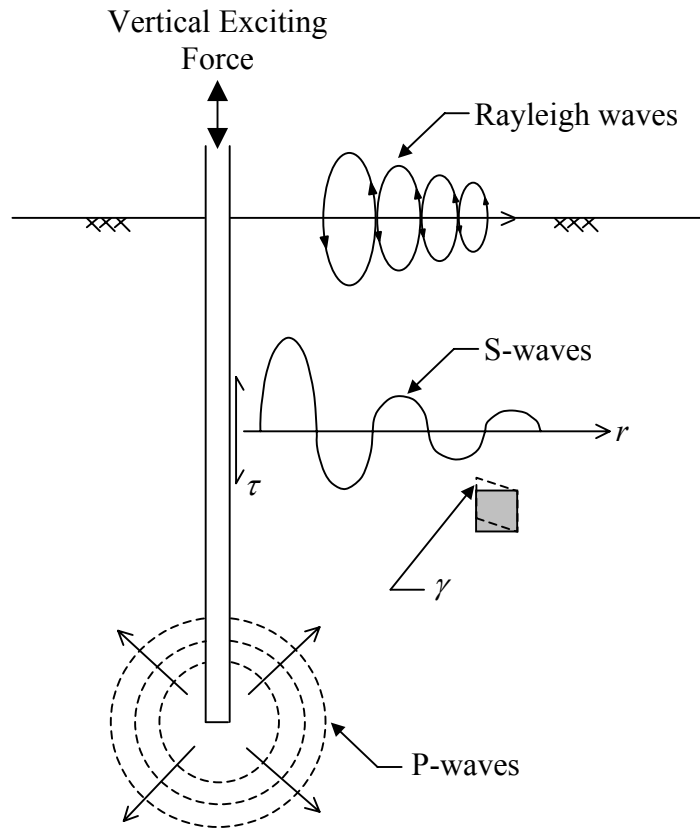
Figure 7-13. Conceptualization of the vibratory probe-soil interaction.

The design of the vibratory probe and procedures for implementation have continually evolved. Brief descriptions of various probe designs are given in the following.

7.2.2.1 Terra-Probe

The Terra-probe method was developed in the United States and consists of a Foster Vibro-driver on top of a 0.76m diameter open tubular probe (pipe pile) (Anderson 1974); see Figure 7-14. The probe is typically 3 to 5m longer than the desired penetration depth and is excited vertically at 15hz. The probe plus vibro-driver weigh approximately 10$tons$. In the case history described by Brown and Glenn (1976), three water jets, consisting of pipes welded to the side of the probe, were used to jet probe in the soil. About 15 probes per hour can be done at a spacing of 1 to 3m. It is of marginal

effectiveness in the upper 3 to 4*m* of the zone densified (Mitchell 1981). In the case history described by Brown and Glenn (1976), vibrocompaction was much more effective in densifying the soil than the Terra-probe method.

Figure 7-14. Terra-Probe, not to scale. (Adapted from written description given in Brown and Glenn 1976).
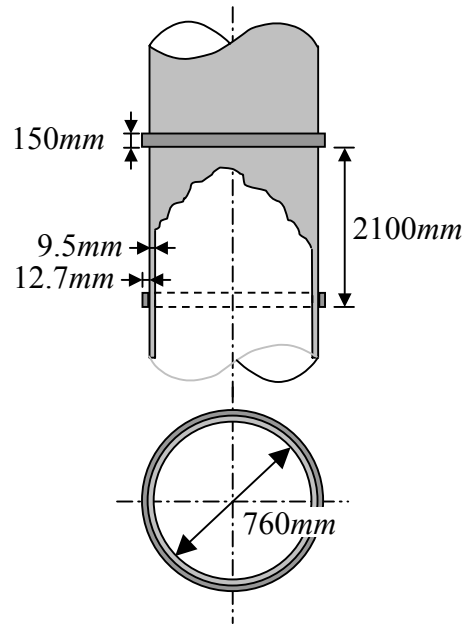
7.2.2.2 Double Tube Rod and Rod with Projectives

Saito (1977) describes a case history where the vibratory probes shown in Figure 7-15 were used to densify reclaimed land. A vibratory pile driver was used to excite the probes, and the technique of repeated insertion and withdrawal of the probe was used to densify the soil to a depth of 8*m*. Saito (1977) does not give details about the frequency of excitation or the spacing of the compaction points. However, several figures are shown comparing the increases in penetration resistances resulting from the vibratory probe method and vibrocompaction. The vibratory probe method appears to have been more effective in densifying the soil than vibrocompaction.
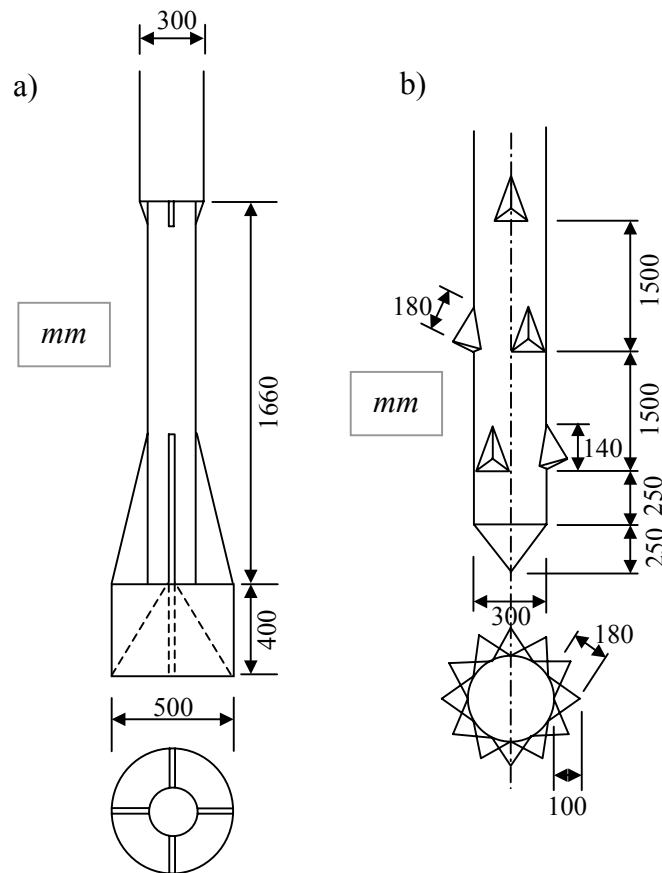
Figure 7-15. a) Double rod probe, and b) Probe with projectives. (Adapted from Saito 1977).

Saito (1977) also presents a figure showing the effectiveness of the vibratory probe method as a function of the fines content of the soil, shown below as Figure 7-16. As may be observed from this figure, the increase in SPT N-values due to treatment decreases as the fines content increases. This phenomenon is likely due to the inability of silty soils to rapidly dissipate excess pore pressures once liquefaction is induced.

Figure 7-16. Penetration resistance of pre- and post-treated soil as a function of fines content. (Adapted from Saito 1977).
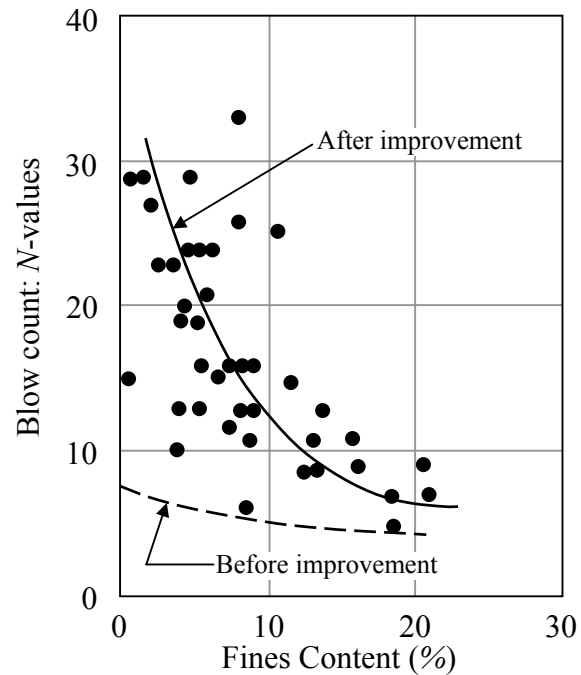
7.2.2.3 Vibro Wing

The vibro-wing was developed by a Swedish contractor and consists of a heavy vibrator (7*tons*) attached to the top of an approximately 15*m* long steel rod. Protruding from the rod are approximately 0.8*m* long wings, spaced at about 0.5*m* (Figure 7-17). The vibratory hammer is operated by heavy crane, normally used for the installation of prefabricated concrete piles. The probe is driven into the ground down to the desired depth of compaction. If necessary, the driving can be facilitated by jetting at the bottom of the probe. The probe is then vibrated vertically until the required degree of compaction has been reached. The frequency of vibration is typically 20*hz* but can be varied to fit the conditions at the particular site. The duration of vibration and rate of withdrawal of the probe depends mainly on the permeability of the soil, the depth of the deposit, and the spacing of the compaction points. Additionally, the pull-out resistance of the probe can be monitored during the compaction by a load cell placed at the top of the crane. (Massarsch and Linberg 1984; Massarsch and Broms 1983)

254

Massarsch and Linberg (1984) and Massarsch and Broms (1983) describe a case history where the vibro-wing was used to densify a 10 to 15m thick deposit of hydraulic fill consisting uniform loose fine sand with the ground water table at a depth of 0.5m. A triangular grid pattern was used with 2.5m spacings between the compaction points. The duration of the compaction at each point was about 5 minutes. On average the penetration resistance increased 300 to 700 percent as a result of treatment (e.g., at a depth of about 5m the CPT tip resistance increased from about 3MPa before treatment to 20MPa after treatment).
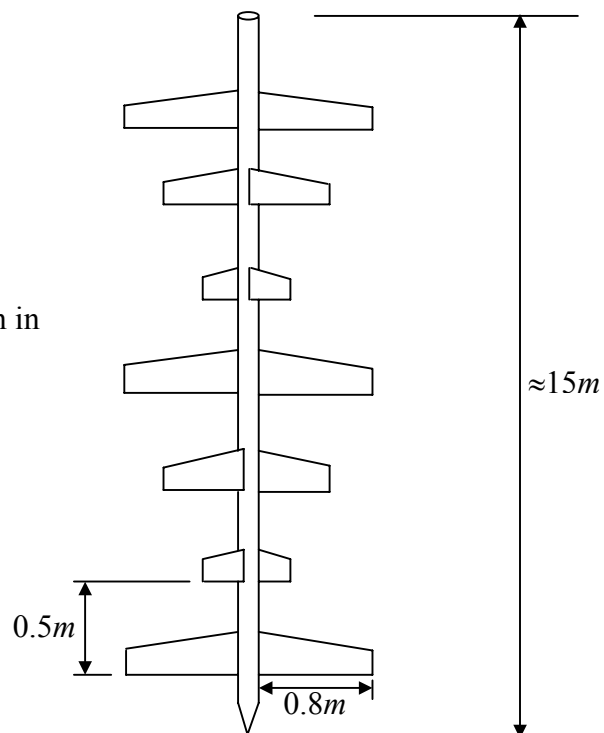
Figure 7-17. Swedish vibro-wing. (Adapted from a photograph shown in Massarsch and Broms 1983).

≈15m

0.5m

0.8m

7.2.2.4 Franki TriStar Probe (or Y-Probe)

The TriStar probe was developed and patented in the late 1970's and consists of three long steel plates 500mm wide and 20mm thick, which are attached to a long steel rod 15 to 20m long. The steel plates are oriented such that they are 120° to each other. Additional steel ribs 300mm × 50mm × 10mm are welded to both sides of each plate at 2m intervals to further improve the efficiency of the probe; see Figure 7-18. A variable frequency piling vibrator is mounted on top of the probe and delivers vertical vibrations

at a frequency ranging from 5 to 20hz. The degree of improvement that can be achieved
for a given soil depends mainly on the duration of vibrations, the frequency, and the rate
of withdrawal of the probe, the spacing between compaction points, and the fines content
(permeability) of the deposit. (Van Impe et al. 1993)

Neely and Leroy (1991) present the post-treatment penetration resistances as a function
of the tributary area of the compaction points for both the TriStar probe and
vibrocompaction. No specifics on compaction times or site conditions are given, but the
TriStar probe appears to have been more effective at densifying the soil than
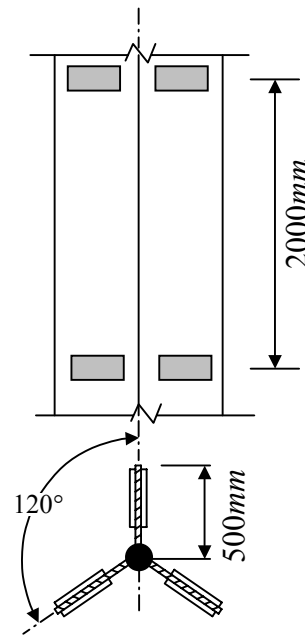vibrocompaction.

Figure 7-18. Franki TriStar probe or Y-probe. (Adapted from Van Impe et al. 1993).

7.2.2.5 Double-Y or Flexi Probes

The double-Y or Flexi probes, shown in Figure 7-20, are designed to take advantage of
observed vibration levels produced from pile driving. Wiss (1967) developed the
following empirical expression relating peak particle velocity occurring at distance D
from the pile tip and impact hammer energy per blow.

$$v = K \frac{\sqrt{E}}{D} \qquad\qquad (7\text{-}2)$$

where: v =   Peak particle velocity of induced vibrations at distance D from the pile tip (*mm/sec*).

            K =   Empirically determined constant.

            E =   Hammer energy per blow (*Joules*).

            D =   Distance from the pile tip (*m*).

Heckman and Hagerty (1978) presented the correlation shown in Figure 7-19 relating the empirically determined *K*-factor to the impedance of the pile (*I*), where *I* is defined by the following expression (Peck et al. 1974).

$$I = \frac{E_y A}{c} \qquad\qquad (7\text{-}3)$$

where: I =   Pile impedance.

            E_y =   Young's modulus of pile.

            A =   Cross-sectional area of pile.

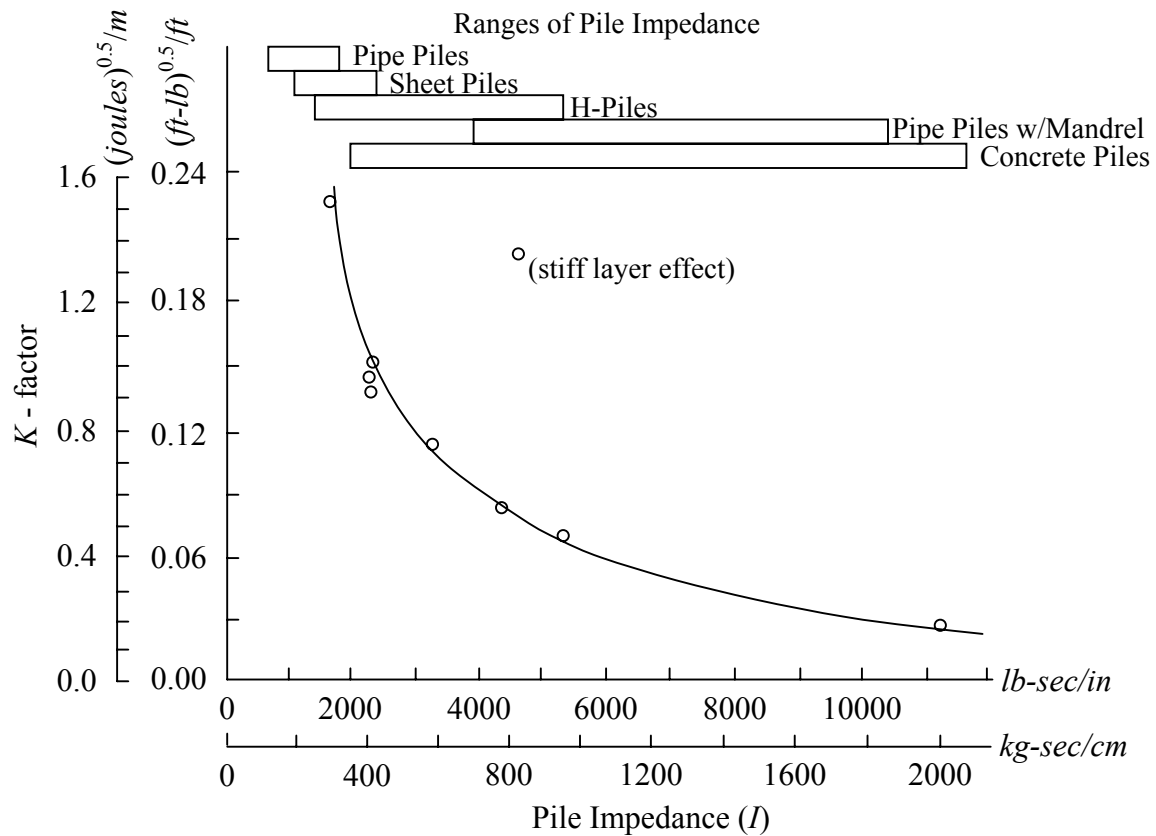 c =   Rod wave velocity of the pile.

Figure 7-19. *K*-factor as a function of pile impedance. (Adapted from Heckman and Hagerty 1978).

From Equations (7-2) and (7-3) and Figure 7-19, piles and equipment can be selected to control the amplitude of the vibrations produced during pile driving. However, these expressions and correlations may also be used to design vibratory probes to maximize the amplitude of the induced vibrations for soil densification purposes. In this vein, a probe was designed with cutouts that decreased its effective cross sectional area and therefore decreased its impedance. As may be observed from Figure 7-19, decreasing the pile (or probe) impedance results in larger *K*-factors and hence increased soil vibrations. However, the geometry of the probe had to be such that it remained elastic during loading. The result is the double-Y or Flexi probe, a conceptual drawing of which is shown in Figure 7-20 (Van Impe and Madhav 1995).

258

Cutouts used to reduce the effective area of the probe and therefore reduce its impedance
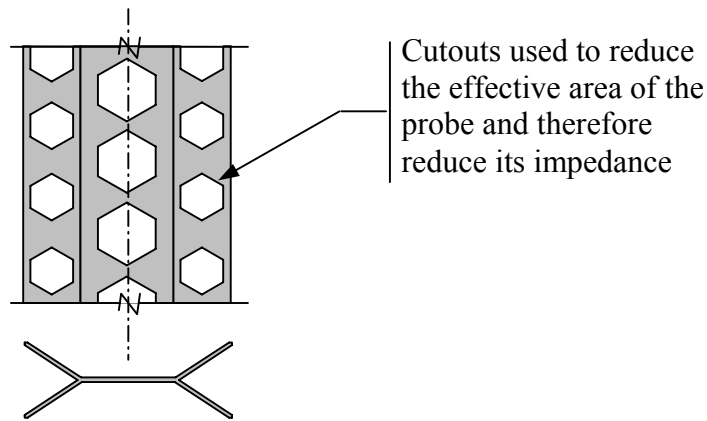
Figure 7-20. Double-Y or Flexi probe. Not to scale; no dimensions given. (Adapted from a photograph presented in Van Impe et al. 1994).

Heckman and Hagerty (1978) define D as "the distance to the hammer," as opposed to Wiss (1967) who defined D as the distance to the pile tip. It is uncertain whether this inconsistency is actual or whether it is simply a misstatement in Heckman and Hagerty (1978). Along this same line, Equation (7-2) is inconsistently presented in Wiss (1967) as:

$$v = K \frac{\sqrt{E}}{D} \qquad \text{and} \qquad v = K \sqrt{\frac{E}{D}}$$

(i.e., it is presented both ways in the same paper). Unfortunately, this inconsistency was perpetuated in Heckman and Hagerty (1978) and several more recent publications (i.e., in one paragraph it is presented one way and in another paragraph it is presented the other). Personal communication with Hagerty (2001) leads the author to believe that the correct expression is as presented as Equation (7-2). Regardless of the correct form of Equation (7-2) or the definition of D, the trend between the amplitude of the induced vibrations during driving and pile impedance is clear: as pile impedance decreases, the amplitude of the induced vibrations during driving increases. It is this general trend on which the design of the double-Y probe is based.

7.2.2.6 Frequency of Vibration

In addition to optimizing the design of the probe, studies have been conducted regarding the influence of the excitation frequency on soil densification. The results of one such study on an $8m$ deep deposit of saturated silty-fine sand are shown in Figure 7-21. The compaction points were arranged in a triangular grid pattern, and the post-treatment penetration resistances were measured at the centers of the compaction points. A clear trend in the data can be observed showing higher penetration resistances for the soil densified at $14hz$ than for the soil densified at $17hz$ (Massarsch 1991). This is in spite of the amplitude of the vibratory force being less at $14hz$ than $17hz$, as may be determined from the following expression.

$$Q = m_e e \omega^2 \qquad \text{(e.g., Richart et al. 1970)} \qquad (7\text{-}4)$$

where: Q = Amplitude of the vibratory force.

m_e = Total mass of the counter-rotating masses.

e = Eccentricity of the counter-rotating masses.

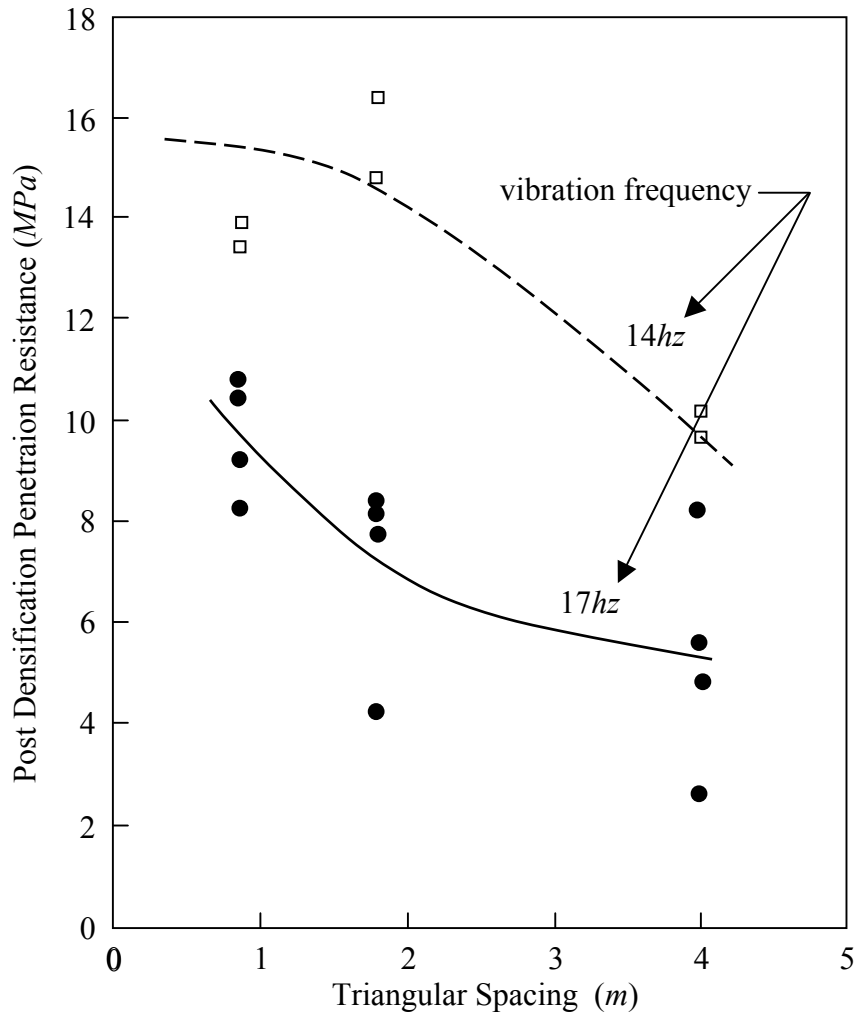ω = Vibration frequency (*rad/sec*).

Figure 7-21. Results from study comparing the influence of vibratory frequency on densification. (Adapted from Massarsch 1991).

As given in Massarsch and Heppel (1991), the optimal frequency for compaction can be determined by performing a spectral analysis of a velocity time history recorded while the vibrator is switched on or off. As the probe is switched on or off, all the frequencies from zero to the maximum operating frequency of the vibrator are excited. A typical velocity time history recorded at a distance of 3.5*m* from the probe as the vibrator was switched on is shown in Figure 7-22.
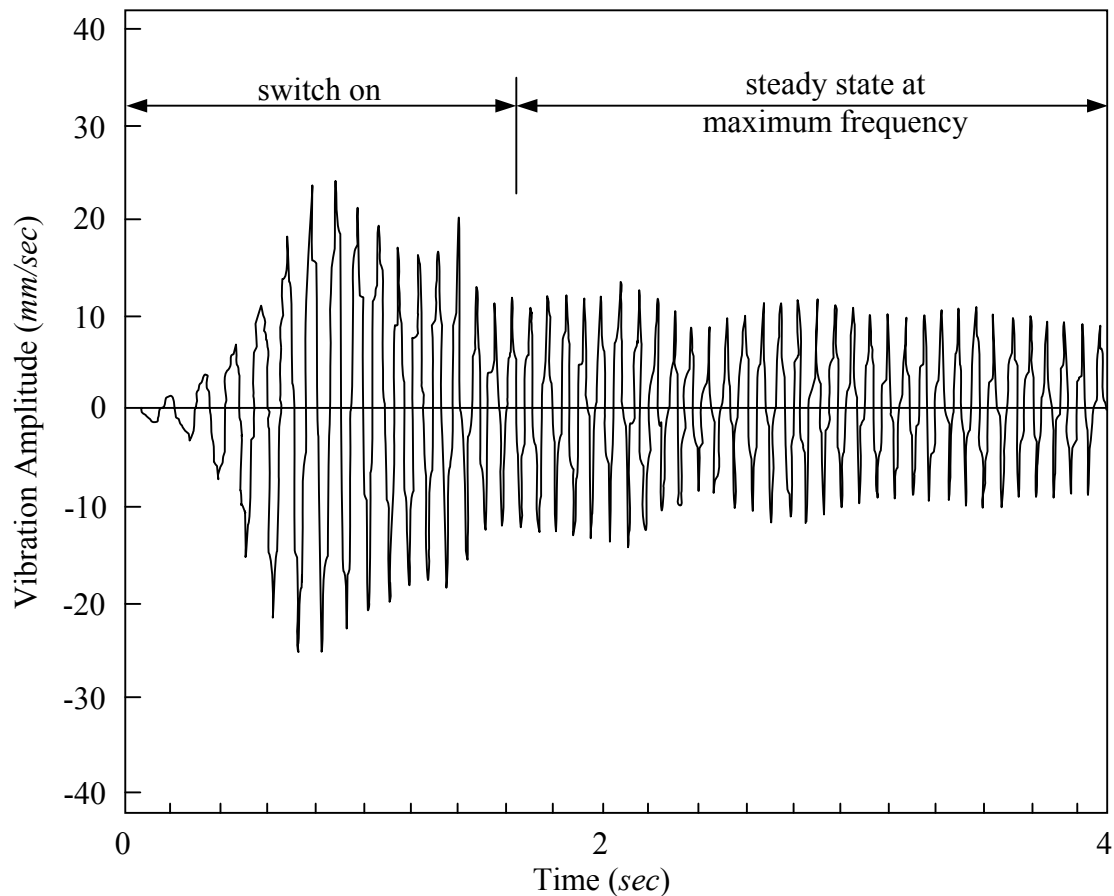
Figure 7-22. Velocity time history recorded at 3.5*m* from the vibratory probe during switch on. (Adapted from Massarsch and Heppel 1991).

From this figure, it can be observed that the maximum recorded velocity occurs before steady state is reached, implying that the resonant frequency of the system is lower than the maximum operating frequency of the vibrator. The frequency spectra of vertical peak particle velocities for the TriStar probe (or Y-probe) and the Flexi probe (or double- Y probe) are shown in Figure 7-23. As may be seen in this figure, the optimal frequencies for densification are approximately 16 and 14*hz* for the Y- and double-Y probes, respectively.
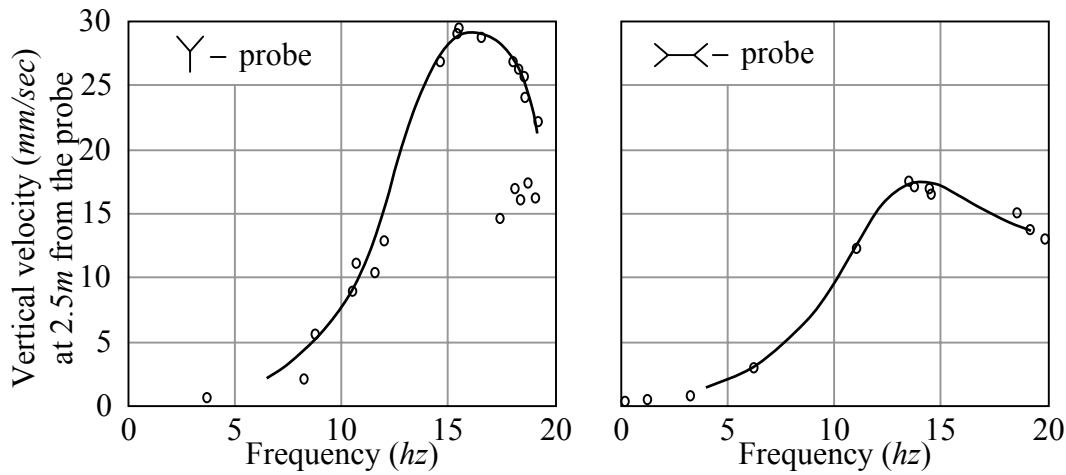
Figure 7-23. Frequency spectra of vertical peak particle velocities for the Y- and double-Y probes. (Adapted from Van Impe et al. 1994).

Although Figure 7-23 shows a clear variation of the vibration amplitude as a function of frequency, the author surmises that the "optimal frequency" determined by this approach is inherently linked to the distance at which the velocity transducer is placed from the probe. This can be understood by examining Figure 7-24. If only SV-waves are considered, the exciting frequency that causes the largest particle velocity at a distance H from the probe, most likely corresponds to that having a quarter wavelength of H.

$$\frac{\lambda}{4} = H = \frac{v_s}{4f} \qquad \text{(e.g., Richart et al. 1970)} \qquad (7\text{-}5)$$

where:　λ　=　Wave length.

　　　　H　=　Distance from probe to velocity transducer.

　　　　v_s　=　Shear wave velocity of soil.

　　　　f　=　Vibration frequency (hz).

Although in actual field conditions the generation of P- and Rayleigh waves and the restraints placed on the soil by the underlying bedrock further complicate the situation, the same principle between distance-optimal frequency still applies. If the author's

hypothesis is correct, the excitation frequency should be selected such that vibrations are maximized at some distance from the probe, which should likely be a function of the spacing of the compaction points. Massarsch and Heppel (1991) do not specify the distance at which the transducer should be placed from the probe, but rather just present the results from studies where the distance ranged from 2.5 to 3.5m.
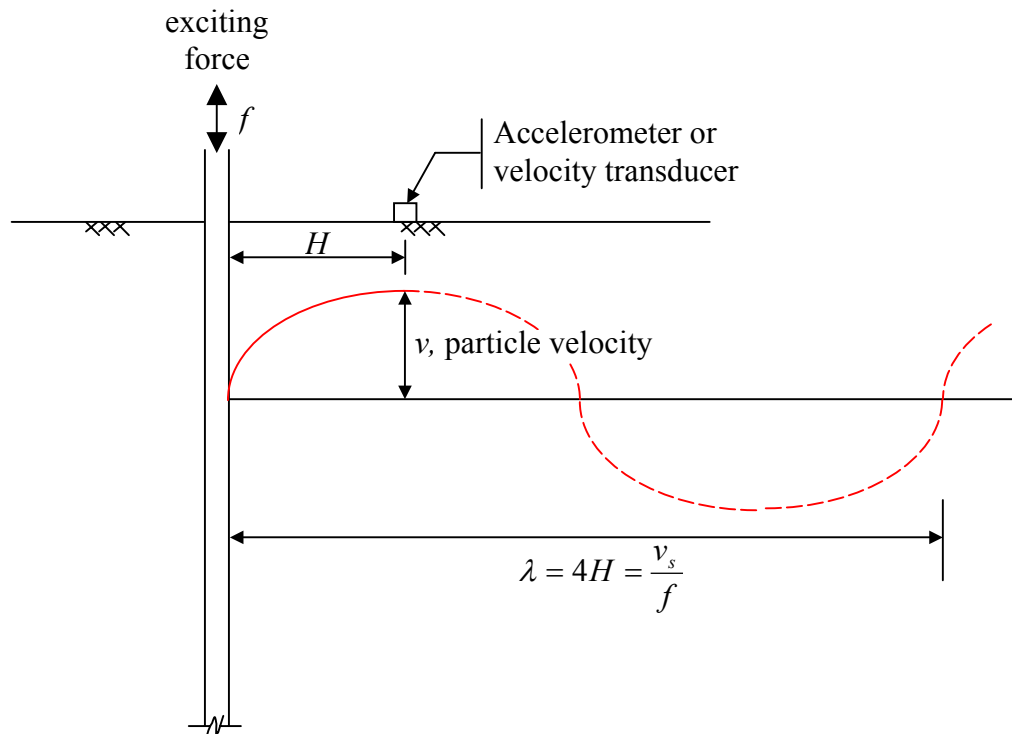

Figure 7-24. Relationship between optimal vibration frequency and the distance between velocity transducer and probe.

Regardless of the distance between the probe and transducer, by using a vibratory probe having low impedance and exciting it at the resonant frequency of the probe-soil system, a maximum transfer of energy from the vibrator to the soil can be achieved. Muller Geosystems, a European based geotechnical firm, markets equipment and services for employing the procedure presented by Massarsch and Heppel (1991) for densifying the soil at the resonance frequency of the soil-probe system, referred to as the Muller Resonance Compaction (MRC) System.

The following figures appear in a Muller Geosystems report (i.e., Massarsch and Heppel 1991) and are used in the preliminary design of densification programs using the MRC System. The soil types applicable for vibratory probe densification as functions of the CPT tip resistance and sleeve friction ratio are shown in Figure 7-25.
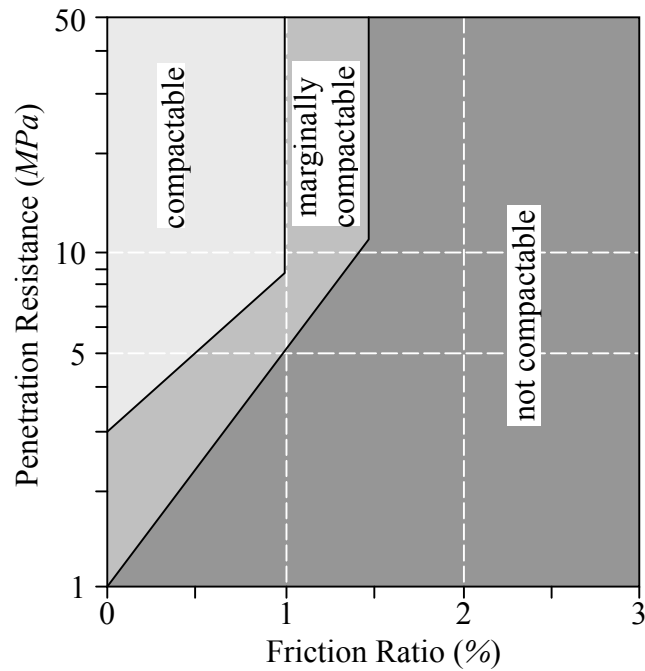
Figure 7-25. Compactability of soils for the vibratory probe technique, based on the electric cone penetration test (CPT) with friction sleeve measurements. (Adapted from Massarsch and Heppel 1991).

To assist in the selection of the size of the vibrator, Massarsch and Heppel (1991) present the semi-empirical correlation shown in Figure 7-26 relating initial penetration resistance, layer thickness, and the vertical peak ground acceleration required to densify the soil.

265
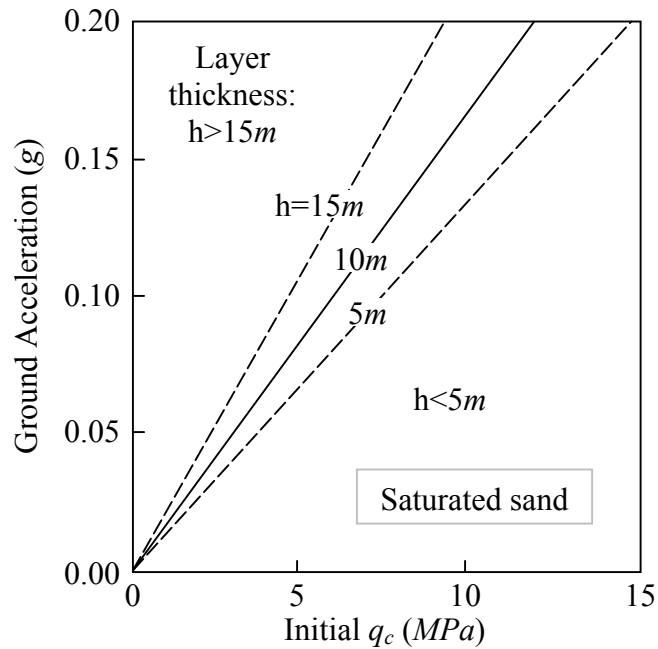
Figure 7-26. Correlation relating initial penetration resistance, layer thickness, and the required vertical peak ground acceleration to densify the soil. (Adapted from Massarsch and Heppel 1991).

Finally, a correlation is shown in Figure 7-27 relating peak ground acceleration, initial penetration resistance, and average induced settlement as a result of densification of the soil. By using these correlations, preliminary designs of densification programs can be made.

Figure 7-27. Correlation relating the peak ground acceleration, initial penetration resistance, and average induced settlement of treated layer. (Adapted from Massarsch and Heppel 1991).
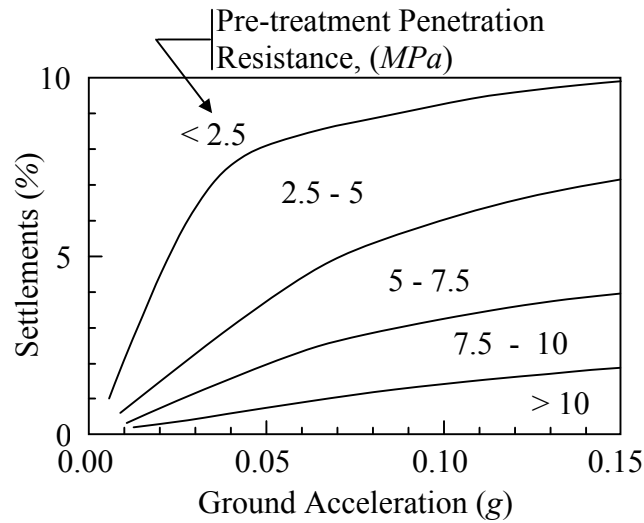
Unfortunately, Massarsch and Heppel (1991) do not provide any supporting data for the design aids shown in Figures 7-25, 7-26, and 7-27.

7.3 Deep Dynamic Compaction

Deep dynamic compaction consists of the repeated dropping of heavy weights (or tampers) on the ground being densified. Although the origin of this technique dates back to the Romans, it became formalized as an approach for ground densification in the late 1960's and has been referred to in literature as heavy tamping, dynamic consolidation, and deep dynamic compaction (Elias et al. 1999). The technique is illustrated conceptually in Figure 7-28. The mass of the tamper generally ranges from 5.4 to 27.2Mg, and drop height ranges from 12.2 to 30.5m (Lukas 1995).

W = Mass of tamper.

H = Drop height.

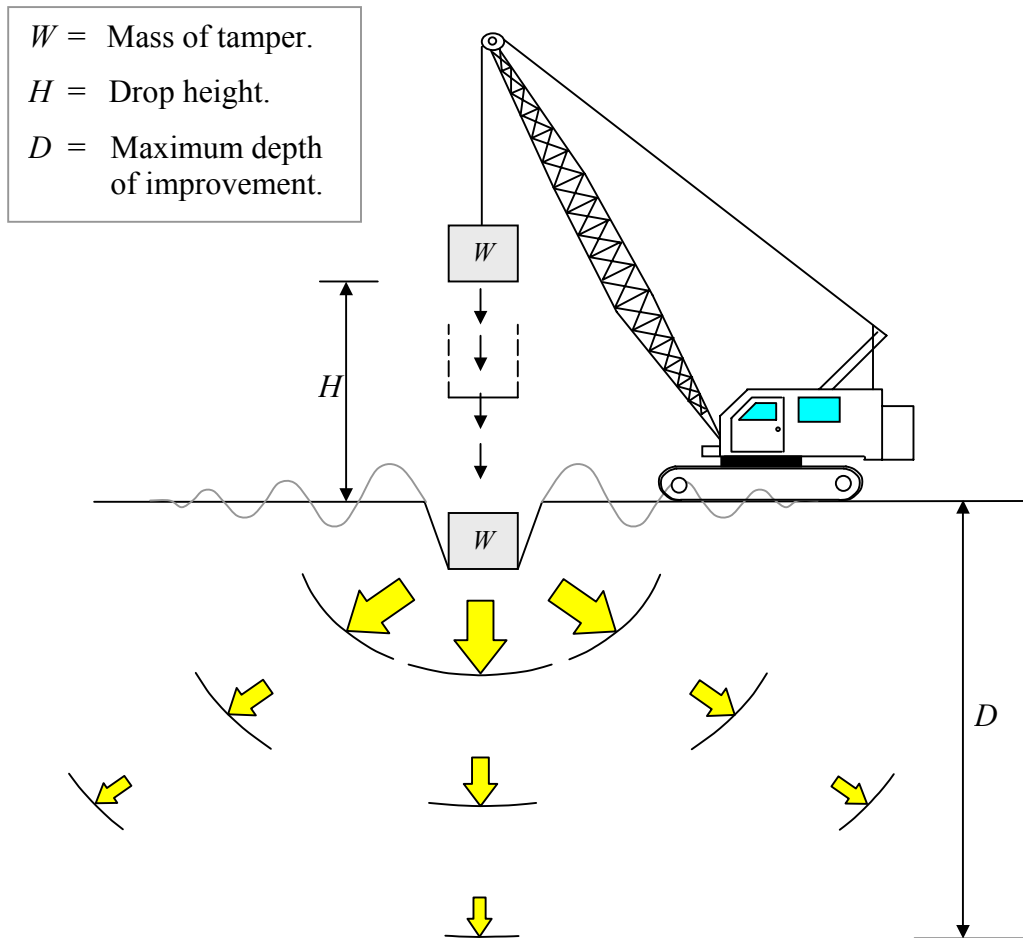D = Maximum depth of improvement.

Figure 7-28. Conceptual illustration of deep dynamic compaction. (Adapted from Lukas 1995).

Figure 7-29 shows the range of grain-size distributions applicable deep dynamic compaction. In this figure, soils are classified into three groups: Zone 1, Zone 2, and Zone 3, with Zone 1 soils being the most suitable for deep dynamic compaction and Zone 3 being the least suitable.
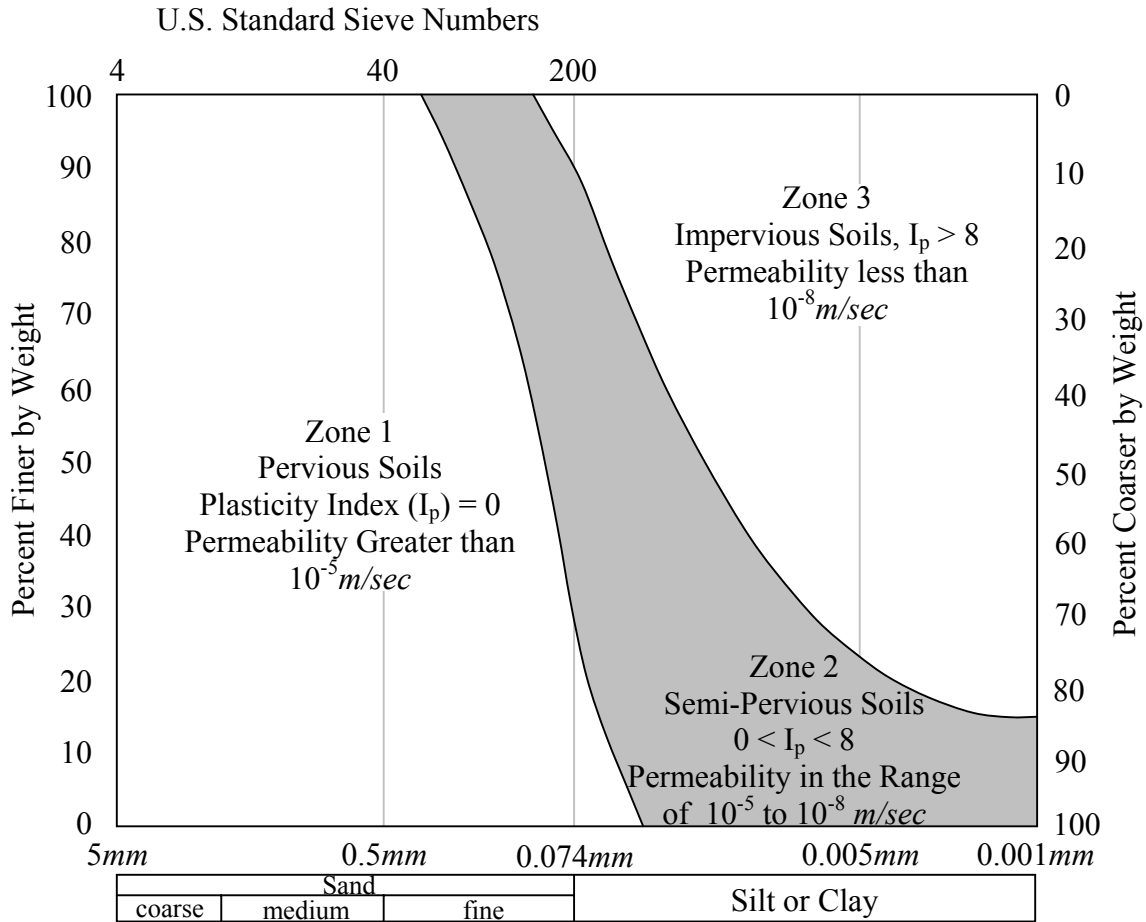
Figure 7-29. Grouping of soils for dynamic compaction. Zone 1 soils are most suitable for deep dynamic compaction. (Adapted from Lukas 1986).

Menard and Broise (1975) gave the following stages that soils progress through as a result of being subjected to deep dynamic compaction:

1. compressibility of saturated soil due to the presence of micro-bubbles;
2. the gradual transition to liquefaction under repeated impacts;
3. the rapid dissipation of pore pressures due to high permeability after soil fissuring;
4. thixotropic recovery.

These stages are illustrated in Figure 7-30, in which each increment of energy represents an additional drop of the tamper. As may be seen in this figure, liquefaction is induced as a result of the weight impacting the ground. Additionally, the bearing capacity of the soil is shown to increase even after the all the excess pore pressures are dissipated. This

phenomenon is referred to as aging and is not unique to deep dynamic compaction, but applies to all techniques that, in the densification process, break down the soil structure (e.g., vibro-compaction and explosive compaction).
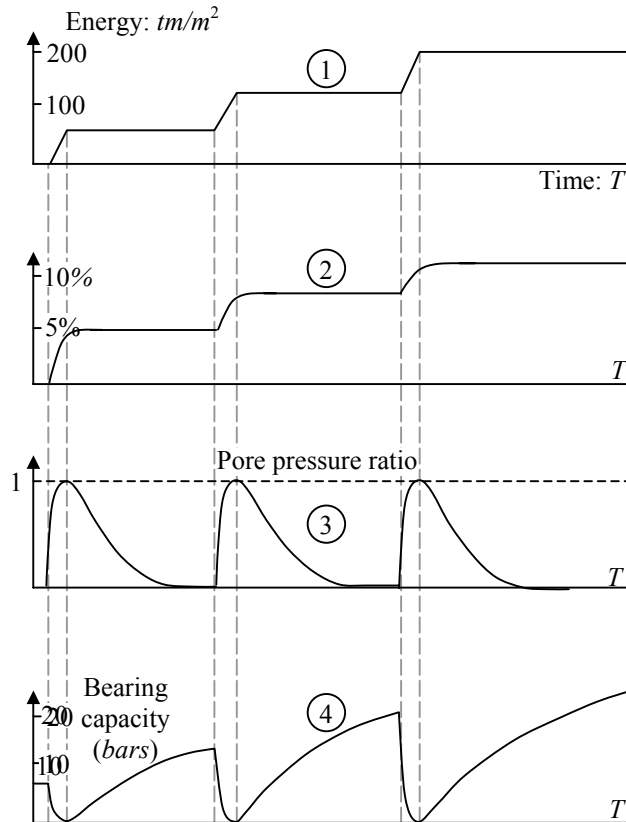
① Applied energy in tm/m^2
② Volume variation with time
③ Pore pressure ratio (r_u)
④ Variation in bearing capacity

Figure 7-30. Stages of soil conditions as a result of successive passes of deep dynamic compaction. (Adapted from Menard and Broise 1975).

Dynamic compaction is generally undertaken using a square grid pattern, similar to that shown in Figure 7-3, with 5 to 15 blows being applied per grid point. Typical spacing between compaction points ranges from 5 to 10m (Van Impe and Madhav 1995). The plan area for compaction typically extends beyond the footprint of the project for a

distance equal to the thickness of the weak deposit being densified (Elias et al. 1999), which is common to most remediation techniques. Often, the proximity of the ground water table or excessive crater depths limits the number of blows that can be applied to a compaction point in succession. Standard practice is to curtail the pounding when the crater depth exceeds one and a half to two times the height of the tamper or when the ground water rises into the crater (ASCE 1997).

As a result of the limited number of sequential drops, densification is usually performed in multiple passes. A pass is the dropping of the weight at designated grid points for a predetermined number of times. "For instance, if the plan is to impart 12 drops at a specific grid location, but only 3 drops could be applied before the crater depths become excessive or ground heaving occurs, the first 3 drops would be called the first pass." (Elias et al. 1999) The next sequence of drops at the same or alternate grid points used in the first pass is the second pass, etc. Following each pass, the craters are either leveled with a dozer or filled with granular fill material before the next pass. In fine deposits, it is sometimes necessary to use 3 or 4 passes, whereas in many cases, only one pass is needed for more previous deposits.

Dynamic compaction may also progress in phases. The first phase of densification uses large masses dropped from greater heights, with greater distances between the drop points. Such initial phases are intended to improve deeper layers, and if performed inappropriately (e.g., too closely spaced drop points), may create a dense upper layer making it difficult or impossible to treat loose material below (ASCE 1997). Completion of the initial "high energy phase" is usually followed by a "low energy phase" (i.e., smaller masses dropped from shorter height), called "ironing," intended to densify the surficial layers in the upper 1.5*m* (5*ft*). During this phase, the tamper is only raised from 5 to 6*m* (15 to 20*ft*) and is dropped on an overlapping grid. (ASCE 1997)

The effects of the high and low energy phases and the effects of aging are illustrated in Figure 7-31. As shown in this figure, the soil near the surface of the profile is actually

loosened to the depth of the craters during the high energy phase. The low energy phase (or ironing) densifies the shallow deposits.
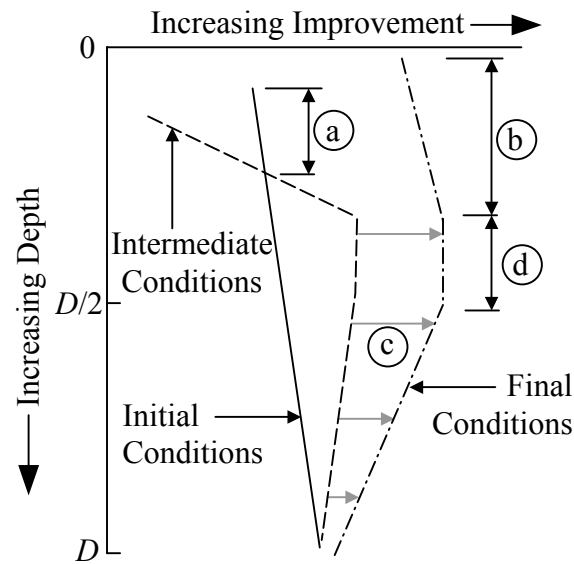
Figure 7-31. The effects of the high and low energy phases of deep dynamic compaction and the effects of aging. (Adapted from Lukas 1995).

The maximum depth of improvement (D) is given by the following expression:

$$D = n \cdot \sqrt{W \cdot H}$$ (7-6)

where: D = Maximum depth of improvement (m).

n = Empirical constant.

W = Mass of tamper (*tonnes*: $1 tonne = 1Mg$).

$$H \quad = \quad \text{Drop height } (m).$$

In this expression, the term $W{\cdot}H$ is proportional to the potential energy of the weight at its drop height. Plots of Equation (7-6) for three different values of n are shown superimposed on actual field data in Figure 7-32.
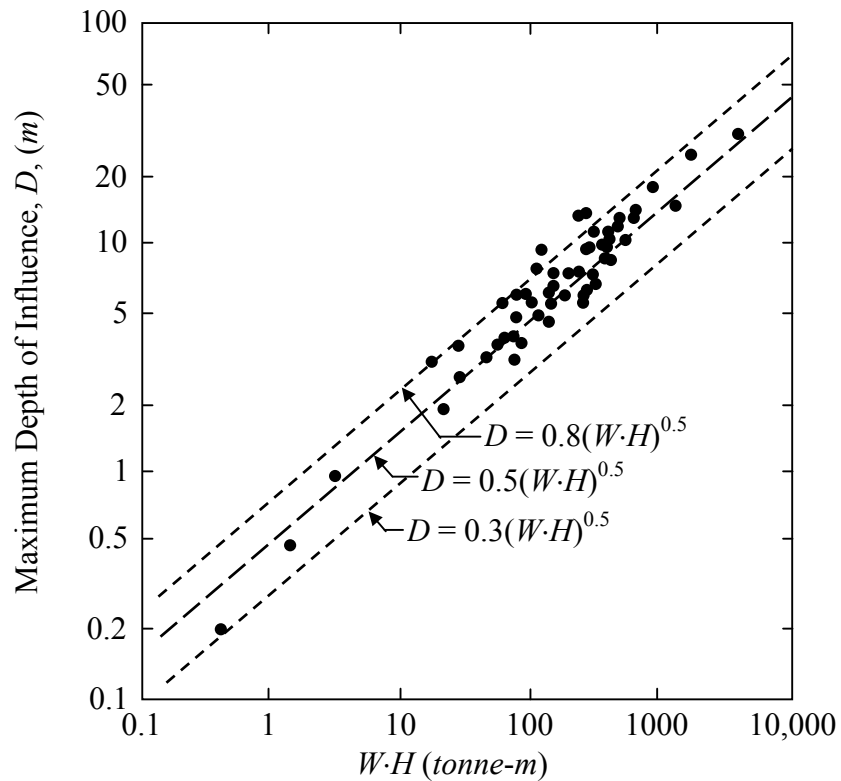
Figure 7-32. Trends between apparent maximum depth of influence and $W{\cdot}H$. (Adapted from Mayne et al. 1984).

The variation of n is attributed to (Lukas 1995):

- Efficiency of the drop mechanism of the crane.
- Total amount of energy applied.
- Type of soil deposit being densified.
- Presence of energy absorbing layers.
- Presence of a hard layer above or below the deposit being densified.
- Contact pressure of the weight against the soil.

273

In general, *n* increases as the permeability of the soil increases. Table 7-3 presents values of *n* from published literature for various soil types and conditions.

Table 7-3. Published values for *n*. (Adapted from Van Impe et al. 1993 and Moreno et al. 1983).

Reference	*n* - values
Menard and Broise (1975)	1.0
Lenards et al. (1980)	0.5
Ramaswamy et al. (1981)	0.6*
Bhandari (1981)	0.51
Charles et al. (1981)	0.35*
Santoyo and Fuentes (1982)	0.37
Bjolgerud and Haug (1983)	1.0 (rockfill)
Smoltczyk (1983)	0.5 (soils with unstable structure) 0.67 (silts and sands) 1.0 (purely frictional soils)
Lukas (1984)	0.65 – 0.8
Mayne (1984)	0.3 – 0.8
Gambin (1984)	0.5 – 1.0
Qian (1985)	0.55 (loess) 0.65 (fine sand) 0.66 (soft clay)
Van Impe (1989)	0.5 (clayey sand) 0.65 (silty sand)

*Values computed by Moreno et al. (1983) from data in listed reference.

As shown in Figure 7-31, the depth to maximum improvement typically ranges from $0.33 \cdot D$ to $0.5 \cdot D$ (Lukas 1995). This range seemingly corresponds to the depth of maximum lateral deflection, as may be observed from Figure 7-33. The data shown in this figure are the result of inclinometer measurements that were obtained at a distance of 3*m* from the centerlines of the drop points. The author hypothesizes that the coincidence of the depths of maximum densification and maximum lateral deflection results from the

large deviatoric shear strains (e.g., Equation (7-1)) that occur at this depth, indicating the significance of lateral deformation in the densification process.

Center of Drop Point: 3*m*

Deflection (*mm*)

Depth (*m*)

B

C

A

A: 15 drops of 16.3*Mg* at 21.3*m* on cohesive mine spoil

B: 12 drops of 27.2*Mg* at 30.5*m* on silty fine sand

C: 15 drops of 15.0*Mg* at 18.3*m* on loose dumped sand
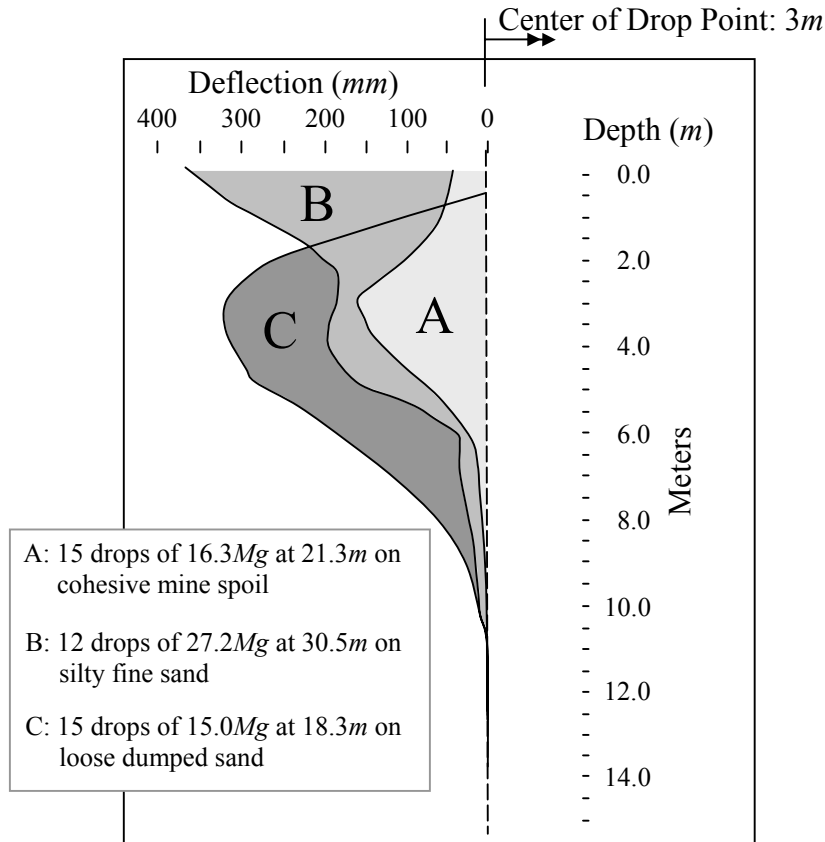
Figure 7-33. Lateral movements 3*m* from the centerlines of the drop points. (Adapted from Lukas 1986).

The cumulative amount of potential energy of the drops applied per unit area of the site may be determined by the following expression:

$$AE = \frac{N \cdot W \cdot H \cdot P \cdot g}{A_{cp}}$$ (7-7)

where: AE = Applied energy (kJ/m^2).

W = Mass of tamper (*tonnes*: $1 tonne = 1 Mg$).

H = Drop height (*m*).

P = Number of passes.

N = Number of drops per pass.

$$g \quad = \quad \text{Acceleration due to gravity } (9.81 m/sec^2).$$

$$A_{cp} \quad = \quad \text{Tributary area per compaction point } (m^2).$$

General guidelines for estimating the amount of energy required for densifying various soils are given in Table 7-4. The heaviest tamper that can be lifted with conventional equipment is about $16 Mg$ with a drop height of 22.9 to 27.4m. This will result in a maximum improvement depth of about 11m. If a greater depth of improvement is required, specialized equipment can be used to lift and drop $27 Mg$ tampers from a height of 30m for a predicted improvement depth of about 14m. (Elias et al. 1999)

Table 7-4. Applied energy guidelines for densifying various soils. See Figure 7-29 for the definitions of the soil Zones. (Adapted from Lukas 1986).

Type of Deposit	Unit Applied Energy (kJ/m^3)	Percent Standard Proctor Energy
Pervious coarse-grained soil (Zone 1)	200 - 250	33 - 41
Semi-pervious fine-grained soils (Zone 2) and Clay fills above the water table (Zone 3)	250 - 350	41 - 60
Landfills	600 - 1100	100 - 180
Note: Standard Proctor energy equals 600 kJ/m^3		

The following steps may be used for initially designing the densification program:

1. Based on Zone of soil, determine energy required for densification from Table 7-4.

2. Knowing the desired depth of improvement (D), use Equation (7-6) to compute $W{\cdot}H$. The appropriate n factor may be estimated from the information listed in Table 7-3. Figure 7-34 may be used to select the specific values of W and H such that desired $W{\cdot}H$ is achieved. Table 7-5 provides information on the required crane size for the selected W.

3. The required number of drops and passes can be estimated using Equation (7-7) such that the imparted energy is greater than the value determined in Step 1 multiplied by the depth of improvement.

Field trials are typically performed to refine the design.
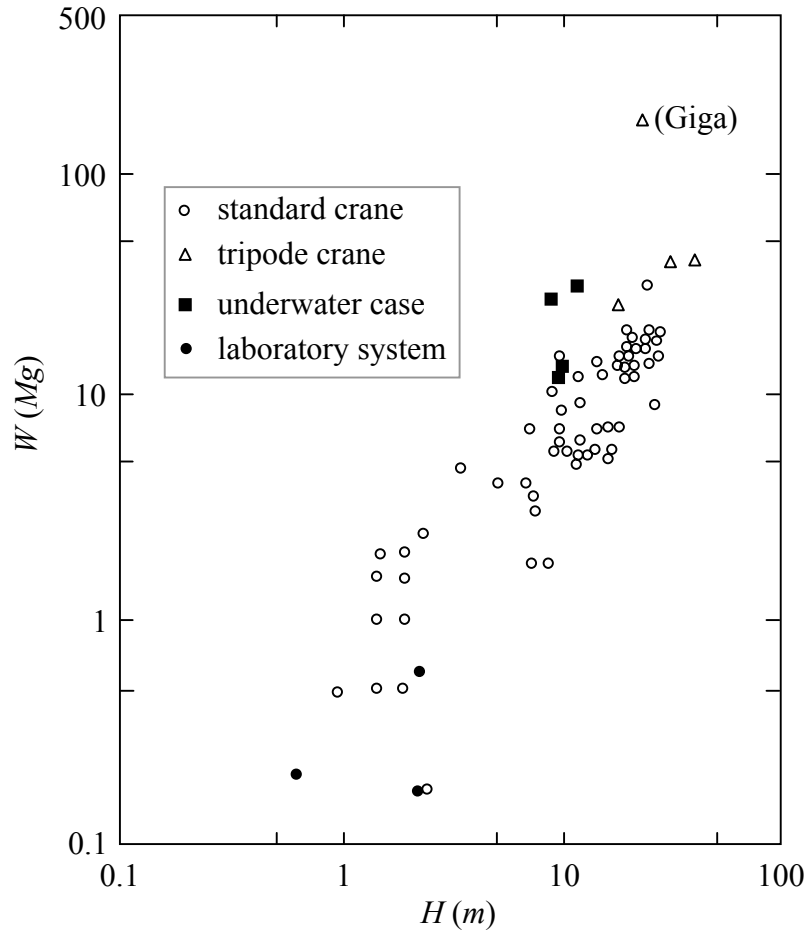

Figure 7-34. Relationship between tamper mass and drop height. (Adapted from Mayne et al. 1984).

Table 7-5. Equipment requirements for different size tampers. (Adapted from Lukas 1986).

Tamper Weight	Crawler Crane Size	Cable Size (*mm*)
3.5 to 7.5*Mg*	40 to 50*tons*	19 to 22
7.5 to 13*Mg*	50 to 100*tons*	22 to 25
13.5 to 16.5*Mg*	100 to 125*tons*	25 to 29
16.5 to 23*Mg*	150 to 175*tons*	32 to 38

The required applied energies for densification are sometimes specified as percentages of the energy applied during a standard Proctor test, as listed in Table 7-4. Although on first appearance deep dynamic compaction seems to be a large-scale Proctor test, the mechanisms of densification and the partition of the imparted energy may be very different. First, the rigid Proctor mold does not allow the same lateral deformation to occur as in the field during deep dynamic compaction. This affects the magnitude of the induced deviator shear strain, which in turn influences the breakdown of the soil structure, especially for saturated soils. Second, even if the same boundary conditions influencing lateral deformation existed, the geometries of the respective tampers do not necessarily have the correct similitude to ensure the proper partitioning of the imparted energy. For an elastic medium, the impact energy is partitioned into P-, S-, and Rayleigh waves. The percentages of the energy carried by these waves are shown in Figure 7-35 for a massless, circular disk sitting on the surface of an elastic halfspace and subjected to harmonic, vertical motions. As may be observed from this figure, the percentage of energy carried by the P-, S-, and Rayleigh waves is dependent on the dimensionless frequency parameter a_o:

$$a_o = \frac{\omega \cdot r_o}{v_s} \tag{7-8}$$

where: a_o =   Dimensionless frequency.

           ω =   Frequency of applied loading (*rad/sec*).

           r_o =   Equivalent radius of tamper and radius of Proctor mass.

$$v_s \quad = \quad \text{Shear wave velocity of the soil.}$$

In this expression, the units of r_o and v_s should be selected such that a_o is dimensionless.

Although the conditions assumed in deriving Figure 7-35 (e.g., harmonic motion of a massless disk on the surface of an elastic halfspace) differ from those for deep dynamic compaction, the author surmises that the general concept of the partitioning of the imparted energy applies to deep dynamic compaction. Furthermore, because the wave types are not equally effective in breaking down the soil structure, proper similitude requires a_o for the Proctor and deep dynamic compaction tampers to be equal.
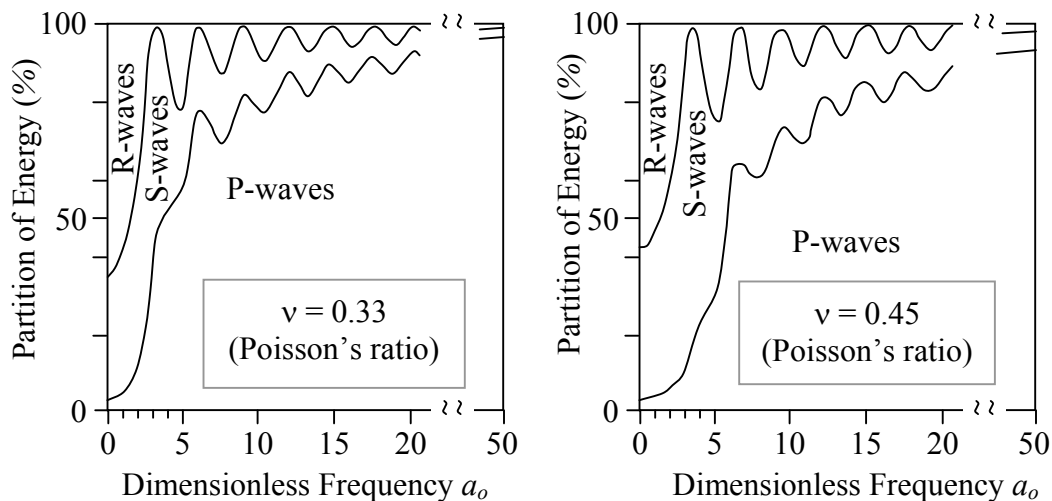
Figure 7-35. Partition of energy among the three waves for vertical vibration of a disk on an elastic half-space. (Adapted from Wolf and Song 1999; also see: Meek and Wolf 1993a,b).

7.4 Explosive Compaction

Similar to deep dynamic compaction, explosive compaction breaks down the soil structure by rapidly imparting energy into the ground. The first successful use of this technique in the United States took place in the late 1930's at a proposed dam site in New Hampshire (Lyman 1942). Even with this early success, the technique is only recently becoming accepted as a viable alternative for remedial ground densification. The reluctance to use explosive compaction stems mainly from concerns about the damaging

effects of the blast-induced vibrations to nearby structures. However, sequencing of detonations has proven to be an effective approach for vibration control, yet allows enough energy to be imparted to the soil to cause liquefaction (Hryciw 1986).

Relatively clean cohesionless soils having initial relative densities less than approximately 50% are best suited for densification by explosive compaction. Soils having initial relative densities greater than approximately 50% may actually loosen from blasting. The maximum achievable post-treatment relative density from blasting is around 80% (Gohl et al. 2000). One advantage of explosive compaction is that it can be used to greater depths than both deep dynamic compaction and vibro-compaction. Soils have been successfully densified at depths up to 40m (e.g., Solymar 1984), with the maximum effective depth of the technique being unknown. As a general rule, larger charges are required at greater depths, and the practical difficulties of placing charges of increasing size at greater depths may be the limiting factor to how deep this technique can be used (ASCE 1997). However, regardless of the depth of treatment, the depth-size relationship of the charge has to be selected such that cratering of the ground surface does not occur.

A typical blasting program consists of charges placed in a grid pattern (e.g., Figure 7-3) spaced at 3 to 8m in developed areas and 8 to 15m in remote areas, with charge weights between 2 and 15 kg (Mitchell and Gallagher 1998). For soil layers less than 10m thick, the charges are usually placed at a depth between one-half and three-quarters the thickness of the layer to be treated, with a depth of two-thirds the layer thickness being common. Layers more than 10m thick are commonly divided into sublayers, where each sublayer is treated separately with decked charges (Narin van Court and Mitchell 1994a). The charges in each sublayer can be set off in sequence from top to bottom or bottom to top, but there is no definitive evidence that one sequence is more effective than the other (Narin van Court and Mitchell 1995).

Surface settlement is almost immediate after the blast, with settlements on the order of two to ten percent the thickness of the treated layer being common. When multiple

passes are employed, the greatest amount of settlement typically occurs with the first pass, and decreases with each additional pass (ASCE 1997). Although the settlement is immediate (i.e., within hours), increases in penetration resistances are usually time dependent and may require several weeks to fully develop (Mitchell and Gallagher 1998).

Three different measures are commonly used to quantify the amount of explosive used in explosive compaction: Hopkinson's Number, normalized weight, and powder factor (Narin van Court and Gallagher 1994b). Hopkinson's Number (HN) is the most commonly used measure and is given by the following expression.

$$HN = \frac{\sqrt[3]{W}}{R} \qquad \text{(7-9a)}$$

where: HN = Hopkinson's Number ($kg^{0.33}/m$).

  W = Weight of charge in equivalent kg of TNT (kg).

  R = Distance from center of charge to point of interest (m).

Hopkinson's Number accounts for the charge weight and distance from the charge, but not the geometry of the charge. As a result, it is better suited to quantify concentrated charges detonated at shallow depths than for columnar or distributed charges used at greater depths.

A better measure to quantify columnar charges is the normalized weight (NW), defined as:

$$NW = \frac{\sqrt{Q}}{R} \qquad \text{(7-9b)}$$

where: NW = Normalized weight ($kg^{0.5}/m^{1.5}$).

  Q = Weight of explosive per meter of charge length (kg/m).

  R = Radial distance from center of the charge column (m).

Finally, the powder factor (PF) is often used to describe the amount of explosive used to treat a unit volume of soil and is defined as:

$$PF = \frac{W}{V} \qquad \text{(7-9c)}$$

where: PF =   Powder factor (g/m^3).

W   =   Weight of charge (g).

V   =   Volume of soil treated by the charge (m^3).

In the subsequent sections, a discussion is given on the mechanisms of the break down of the soil structure, followed by a presentation of several approaches for selecting the size and spacing of the explosive charges.

7.4.1 Mechanisms of Densification

As given by Narin van Court and Mitchell (1995): High explosive charges release large amounts of energy in two distinct forms, shock energy and gas energy. Shock energy results because of the rate of reaction in a high explosive is greater than the speed of sound in the explosive material and forms a shock wave which impacts the surrounding material. The detonation pressure of the explosive refers to the stress applied by the shock wave. The duration of the stresses induced by the shock wave is only a few milliseconds since it propagates through saturated soils at about the same rate as in water, i.e., 1500m/sec (Dowding and Hryciw 1986).

The effect of the shock wave on breaking down the soil structure can be understood by considering the simple case of a spherical charge detonated in a homogenous, isotropically stressed, whole space. Due to the symmetry of the problem, it can most easily be treated using spherical coordinates. The resulting shock wave only induces radial displacements and as such, shears the soil. This can be conceptualized as the inflating of a basketball. As the basketball expands, the rubber shell gets thinner and stretches tangentially. The induced deviatoric shear strain in the rubber shell is proportional to the difference between the radial and tangential strains. The same phenomenon occurs as a spherical shock front propagates radially through the soil. The amplitude of the induced deviatoric shear strain is given by the following expression.

$$\gamma_{dev} = \frac{1}{2} \cdot [\varepsilon_{rr} - \varepsilon_{\theta\theta}] \tag{7-10}$$

where: γ_{dev} =   Deviatoric shear strain.

$\varepsilon_{\theta\theta}$ = Tangential strain in the θ direction.

= Tangential strain in the ϕ direction ($\varepsilon_{\phi\phi}$).

ε_{rr} = Radial strain.

The amplitude of the deviatoric shear strain decreases with increasing distance from the charge. This results from both the decrease in the amplitude of the particle velocity (v) due to geometrical spreading and due to the increase in the radius of curvature of the shock front (i.e., as r increases, the shock wave approximates the one dimensional load case, thus limiting lateral deformation).

In addition to the shock wave, gaseous reaction products induce radial displacements in the soil as the gases expand from the initial volume of the charge to an equilibrium volume with the confining pressures. The stress applied by the expanding gases is called the gas or explosion pressure and typically accounts for 85% of the useful energy released by the explosive for rock blasting (Konya and Walter 1990; McLaughlin 1991). In soils, this proportion may be higher because the gas pressure maintains an elevated stress level for a relatively long time, 0.05 to 0.1sec (Dowding 1985).

As with the shock wave, the radial displacement induced by the gas pressure causes deviatoric shear strains. However, unlike the shock wave, the deviatoric strains induced by the gas bubble cycle as the bubble expands and contacts in an attempt to reach equilibrium with the surrounding pressures (Charlie et al. 1980; Ivanov 1967). The resulting load is similar to that imposed by a cyclic triaxial test. The number of expansion and contraction cycles of the bubble depends on the depth of the detonation, but typically two to four cycles will occur before the gas bubble escapes to the ground surface (Charlie et al. 1980). A schematic illustration of the cyclic nature of the gas bubble is presented in Figure 7-36.

Generally charges are not perfectly spherical nor does the entire charge detonate instantaneously. Rather, the charges have cylindrical shapes and are detonated at one end. The detonation proceeds along the axis of the charge at detonation velocity, V_d, and thus, the shock wave front is conical in shape, as shown in Figure 7-37 (Hryciw 1986).

The contours in this figure show the successive locations of the wave front as the detonation proceeds from the bottom of the charge to the top. The conical shape of the wave front induces additional shear strain in the soil, as illustrated in Figure 7-37.
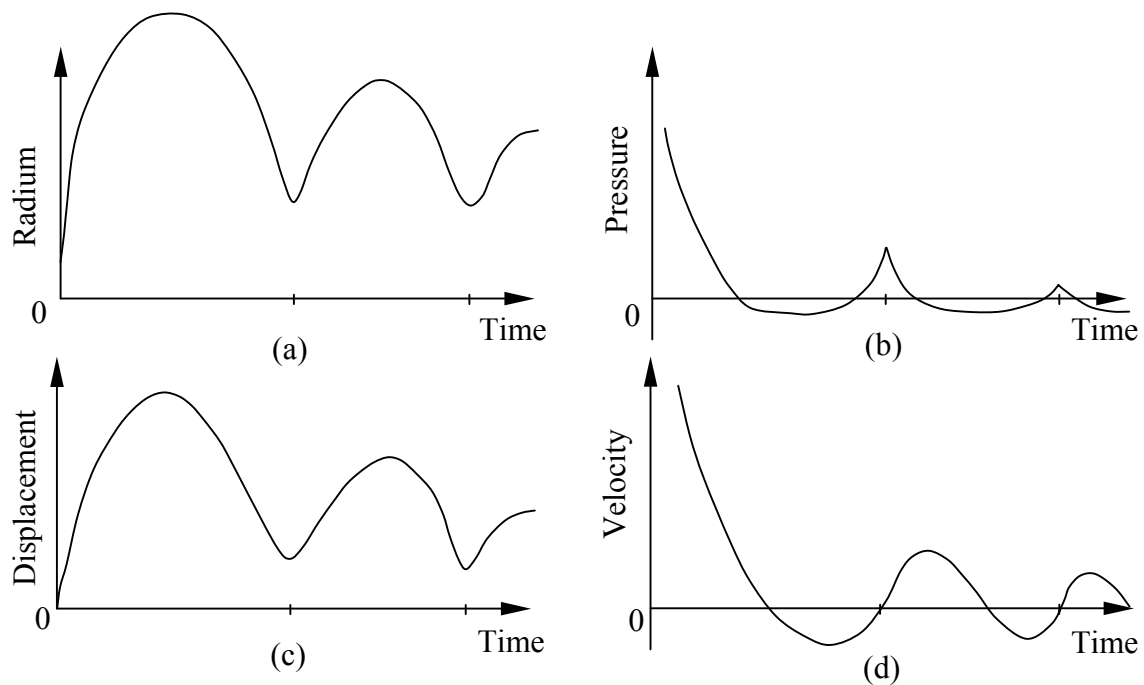

Figure 7-36. Schematic illustration of the times histories from the cyclic expansion and contraction of the gas bubble: a) radius of gas bubble, b) gas pressure, c) displacement of the bubble wall, and d) velocity of the bubble wall. (Adapted from Charlie et al. 1980).
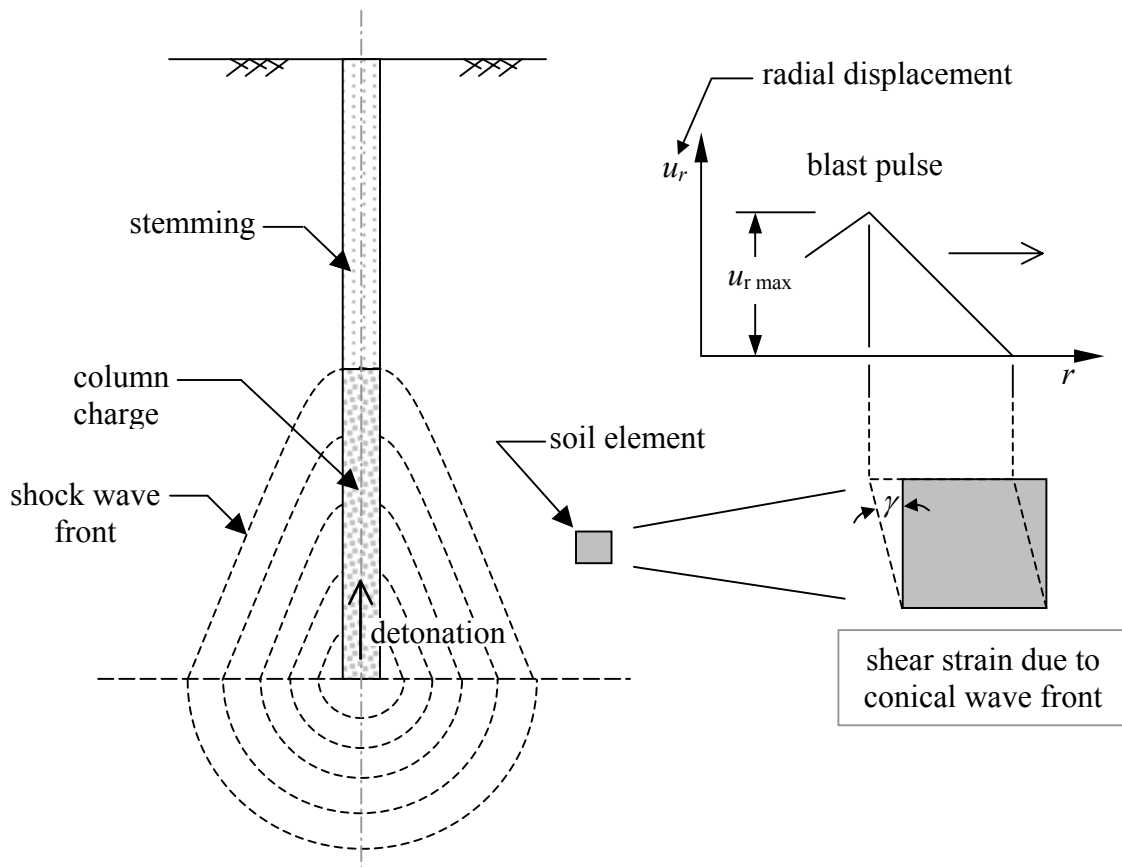
Figure 7-37. Shear strain resulting from the conical shaped wave front. (Adapted from Hryciw 1986).

The amplitude of the induced shear strain is given by the following expression.

$$\gamma_{con} = \frac{v}{V_d} \qquad (7\text{-}11)$$

where: γ_{con} = Shear strain caused by the conical shape of the shock front.

v = Particle velocity of the shock wave.

V_d = Detonation velocity of the explosive.

It should be noted that all of the shear strains discussed above result from compression waves and not shear or Rayleigh waves as described in some publications. Additionally, all occur regardless if the propagation medium is single-phase elastic or multi-phase

anelastic (e.g., saturated loose sand). However, Fragaszy and Voss (1982) proposed an additional mechanism resulting from the differences in the compressibilites of the soil skeleton and the pore water. The change in effective stress may be related to the change in the total stress by Skempton's equations for saturated soil (Skempton 1954):

$$\Delta\sigma'_3 = (1 - B)\Delta\sigma_3 \tag{7-12}$$

where: $\Delta\sigma'_3$ = Change in the effective confining stress.

$\Delta\sigma_3$ = Change in the total confining stress.

B = Skempton's pore pressure parameter.

$$= \frac{1}{1 + n\left(\dfrac{c_w}{m_v}\right)}$$

c_w = Bulk compressibility of water (i.e., $4.67\times10^{-7}m^2/kN$).

m_v = Bulk compressibility of soil skeleton (i.e., soft clay: $2\times10^{-3}m^2/kN$; moderately dense sand: $5\times10^{-6}m^2/kN$).

n = Porosity.

For a porosity of 50% and the values of bulk compressibility of the soil skeleton (m_v) listed above, B ranges from 0.955 for moderately dense sand to 0.9999 for soft clay. For high total stresses, such as induced by the shock wave, plastic volume change occurs in the soil skeleton, resulting in a lower B value for unloading than for loading (i.e., m_v decreases due to the plastic volume change). This phenomenon is insignificant for undrained conditions with low total stresses and is therefore not considered in typical geotechnical analyses. However, from Equation (7-12), the reduction in the B value results in a net decrease in the effective confining pressure after the total stress returns to its original state. If the change in effective confining stress is large enough, liquefaction occurs.

To illustrate this mechanism, Fragaszy and Voss (1982) present the following example. In Figure 7-38, an element of soil is acted on by a total stress of 5MPa, an effective stress of 3MPa, and a pore pressure of 2MPa. The total stress is then increased from 5MPa to

35*MPa*, as shown by the total stress path AB. Assuming *B* = 0.95 (i.e., dense sand), the effective stress will increase from 3*MPa* to 4.5*MPa* (line GH), and the pore pressure will increase from 2*MPa* to 30.5*MPa* (line DE). If the *B* is reduced to 0.75 for unloading as a result of plastic volume change in the soil skeleton that occurred during loading, the pore pressure will decrease more slowly than it rose. As shown in Figure 7-38, liquefaction occurs at 17*MPa*, at which time the effective confining stress equals zero (point I) and the total stress equals the pore pressure (point F).
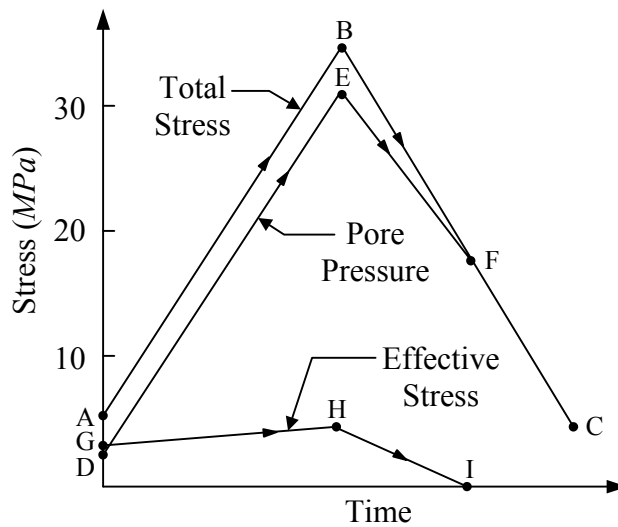

Figure 7-38. Proposed mechanism of blast induced liquefaction resulting from the differences in the bulk compressibilities of the pore water and soil skeleton and the plastic volume change of the soil skeleton. (Adapted from Fragaszy and Voss 1982).

Fragaszy and Voss (1982) verified this proposed mechanism by performing a series of undrained, high pressure, isotropic compression tests on sand. A conceptual illustration of a test result is presented in Figure 7-39.
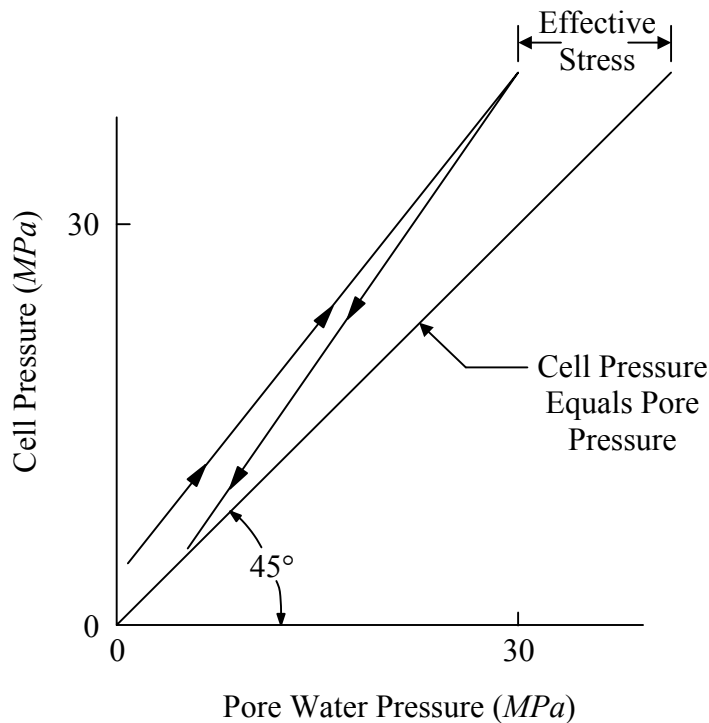
Figure 7-39. Conceptual illustration of undrained, high pressure, isotropic consolidation test that induces liquefaction. Not to scale. Such tests were performed on sands to verify the proposed blast-induced liquefaction mechanism. (Adapted from Fragaszy and Voss 1982).

In actual soil profiles, boundary effects provide further mechanisms for breaking down the soil structure, including the generation of shear and Rayleigh waves as the compressions wave reflect and refract at layer boundaries and at the free surface. Furthermore, anisotropic stress conditions and varying soil stiffness leads to wave dispersion and increases the complexity of blast-soil interaction.

The results of a well-instrumented field study conducted on an offshore loose sand deposit are shown in Figure 7-40 (Kummeneje and Eide 1961). In Figure 7-40a, surface settlements are plotted as functions of the horizontal distance from the blast point for a series of sequential detonations. In Figure 7-40b, the ratio of the settlements of pre- and post-blast screw plate load tests are shown. Ratios less than 1.0 indicate decreased soil strength and stiffness from blasting, while ratios greater than 1.0 indicate increases in

strength and stiffness. No mention is given in Kummeneje and Eide (1961) as to how much time lapsed between the last detonation and the performing of the post-blast screw plate tests. However, given that the maximum surface settlements occurred above the "loosened zones," it is surmised that subsequent plate load tests would have resulted in progressively increasing ratios. Additionally, the non-symmetrical shape of the loosened zone with respect to the blast point is most likely due to the increase in confining stress with depth and the upward migration of blast generated excess pore pressures.
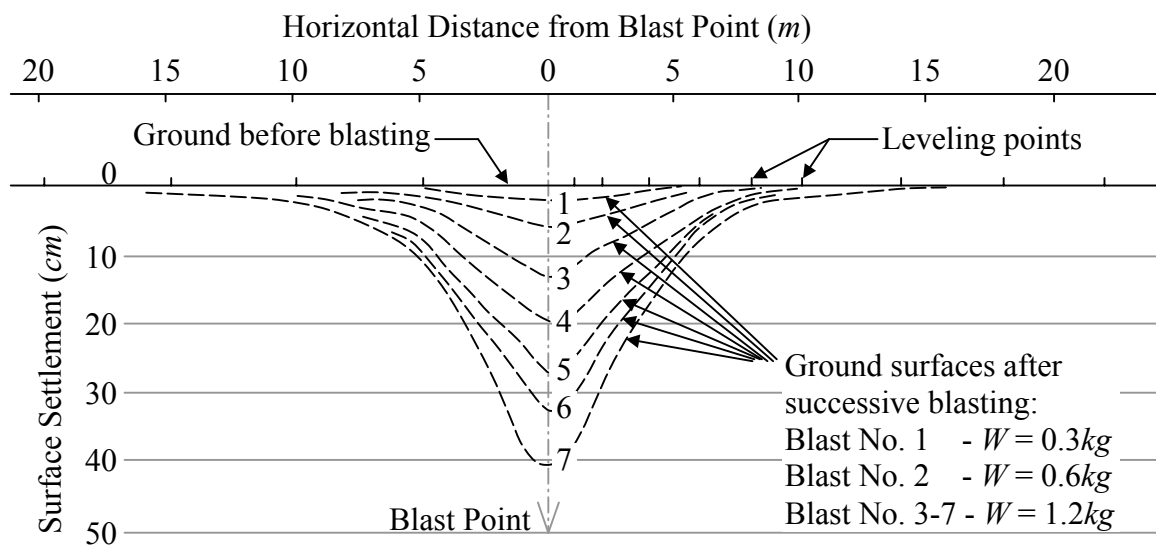

Figure 7-40a. Settlements of the ground surface due to blasting at a depth of $7m$.
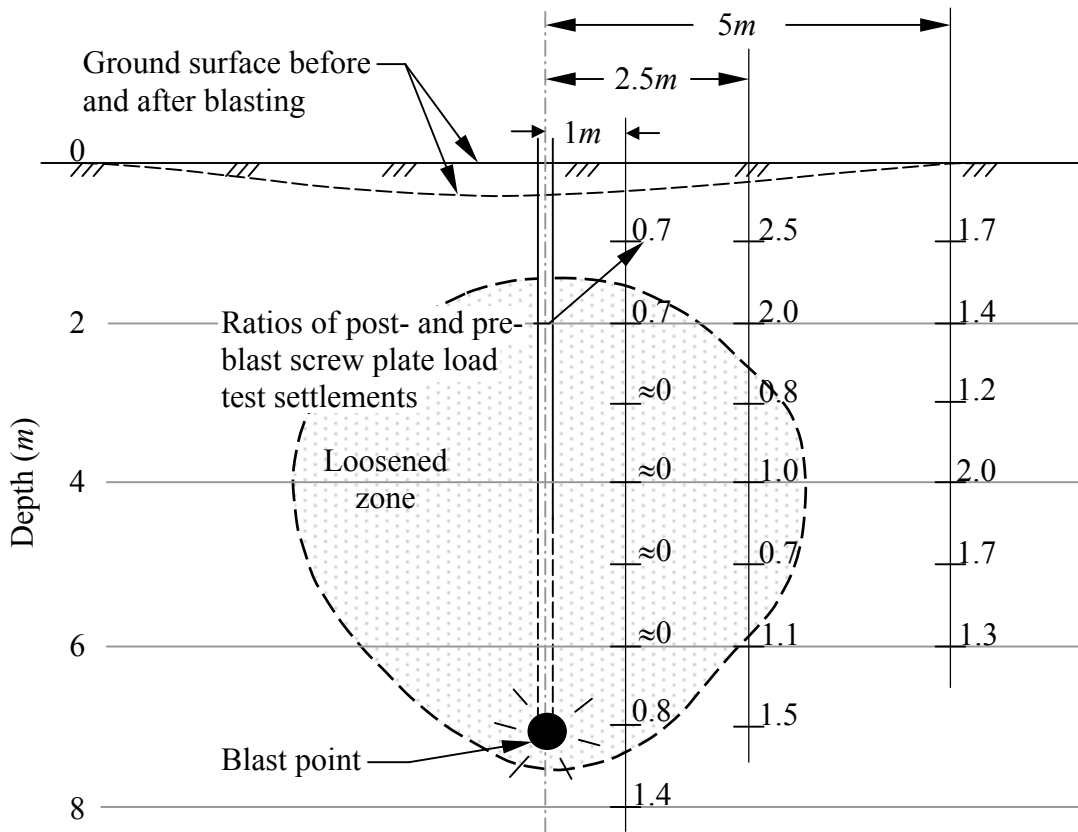(Adapted from Kummeneje and Eide 1961).

Figure 7-40b. Results of pre- and post-blast screw plate load test settlements. Ratios less than 1.0 indicate decreased strength and stiffness, while ratios greater than 1.0 show increases. (Adapted from Kummeneje and Eide 1961).

7.4.2 Procedures for Selecting Charge Size and Spacing

In the following subsections, three approaches for selecting the size and spacing of charges are presented. These parameters are selected such that a desired post-treatment settlement or penetration resistance is achieved.

7.4.2.1 Kok Approach

From field case histories, Kok (1981) presents data relating pore pressure generation and settlements as functions of the energy imparted to the soil, where the energy is specified in terms of the Hopkinson's Number (*HN*), Equation (7-9a).

Figure 7-41 shows the functional relationship between pore pressure and *HN*. In this figure, the generated pore pressures are given in terms of the ratio of the "semi-dynamic excess pore pressure" (Δu_{sd}) and "the original effective stress" (σ').
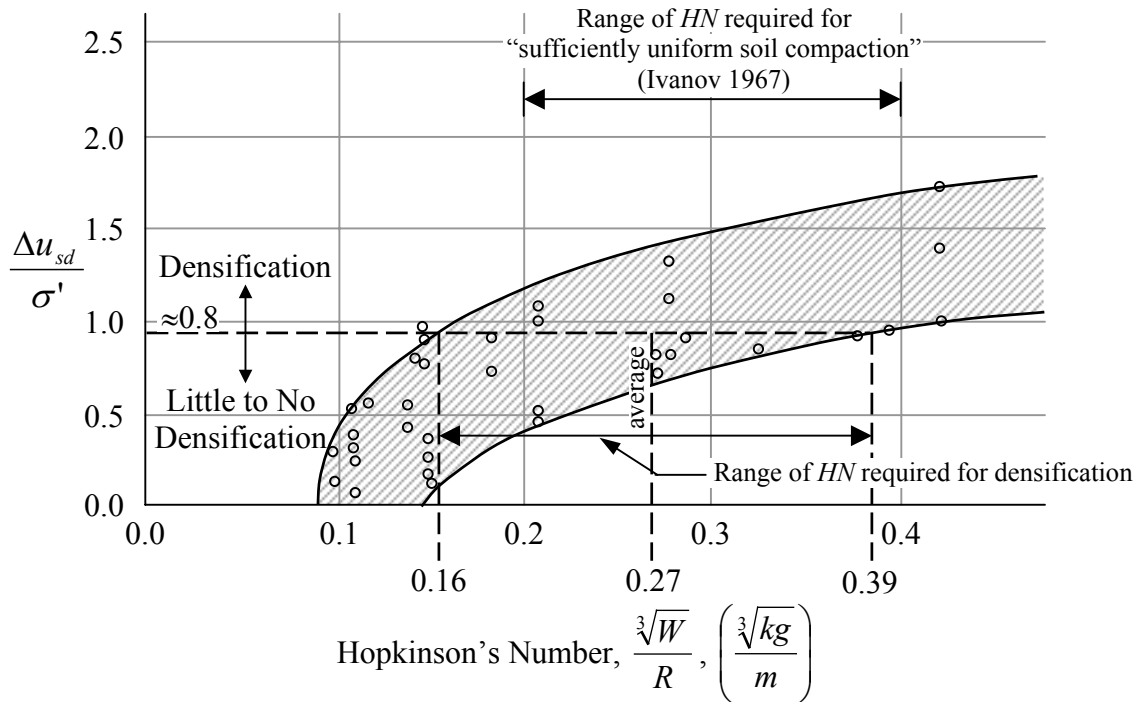
Figure 7-41. Functional relationship between pore pressure ratio ($\Delta u_{sd}/\sigma'$) and *HN*. The above figure was taken from a hand drawn figure, and the scales are not exact. (Adapted from Kok 1981).

Kok and Trense (1979) give the following expressions for the average of the shaded range shown in Figure 7-41, and for the higher and lower boundaries of the shaded range.

$$\frac{\Delta u_{sd}}{\sigma'} = \begin{cases} 0 & for \quad \dfrac{\sqrt[3]{W}}{R} < 0.12 \\[3mm] 1.65 + 0.64 \cdot \ln\left(\dfrac{\sqrt[3]{W}}{R}\right) & for \quad \dfrac{\sqrt[3]{W}}{R} \geq 0.12 \end{cases} \qquad \text{(average)} \qquad (7\text{-}13a)$$

$$
\frac{\Delta u_{sd}}{\sigma'} =
\begin{cases}
0 & \text{for} \quad \dfrac{\sqrt[3]{W}}{R} < 0.09 \\[2ex]
2.15 + 0.74 \cdot \ln\left(\dfrac{\sqrt[3]{W}}{R}\right) & \text{for} \quad \dfrac{\sqrt[3]{W}}{R} \geq 0.09
\end{cases}
\qquad \text{(higher boundary)} \qquad \text{(7-13b)}
$$

$$
\frac{\Delta u_{sd}}{\sigma'} =
\begin{cases}
0 & \text{for} \quad < 0.15 \\[2ex]
1.53 + 0.77 \cdot \ln\left(\dfrac{\sqrt[3]{W}}{R}\right) & \text{for} \quad \dfrac{\sqrt[3]{W}}{R} \geq 0.15
\end{cases}
\qquad \text{(lower boundary)} \qquad \text{(7-13c)}
$$

where: Δu_{sd} = Semi-dynamic pore pressure; see subsequent discussion.

σ' = Original effective stress (same units as Δu_{sd}).

W = Weight of charge in equivalent kg of TNT (kg).

R = Distance from center of charge (m).

As may be seen in Figure 7-41, the minimum value of HN required for generating pore pressures (i.e., $\Delta u_{sd}/\sigma' > 0$) ranges approximately from 0.09 to $0.15 kg^{0.33}/m$. However, for optimal densification efficiency, Kok (1981) specifies $\Delta u_{sd}/\sigma' \geq 0.8$. Using $\Delta u_{sd}/\sigma' = 0.8$ as the criterion for densification, the corresponding range of HN is 0.16 to $0.39 kg^{0.33}/m$, with an average of $0.27 kg^{0.33}/m$. These values were computed using Equation (7-13) and are shown in Figure 7-41. For comparison purposes, Ivanov (1967) specifies a range of HN from 0.2 to 0.4 $kg^{0.33}/m$ for densification, also shown in Figure 7-41. The lower value of Ivanov's range corresponds to fine-grained sand having $0 \leq D_r \leq 0.2$, and the upper value is for medium-grained sand having $0.3 \leq D_r \leq 0.4$.

By knowing the HN required for densification, guidelines can be set for acceptable R-W combinations, such as shown as the dark shaded zone in Figure 7-42. Little to no densification is expected for R-W combinations falling to the right of the acceptable zone, and excessive vibrations and increased likelihood of cratering the ground surface occurs for R-W combinations falling to the left of the acceptable zone.
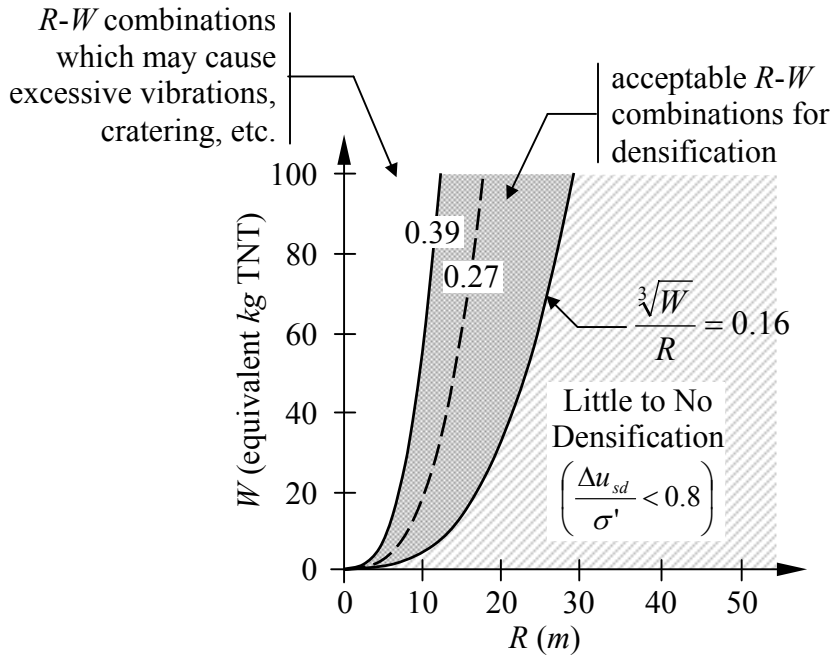
Figure 7-42. Optimal *R-W* combination required for densification is shown as the dark shaded zone.

Again from field case histories, Kok (1981) gives the correlation shown in Figure 7-43 relating vertical strain ($\Delta H/H$) and *HN*.
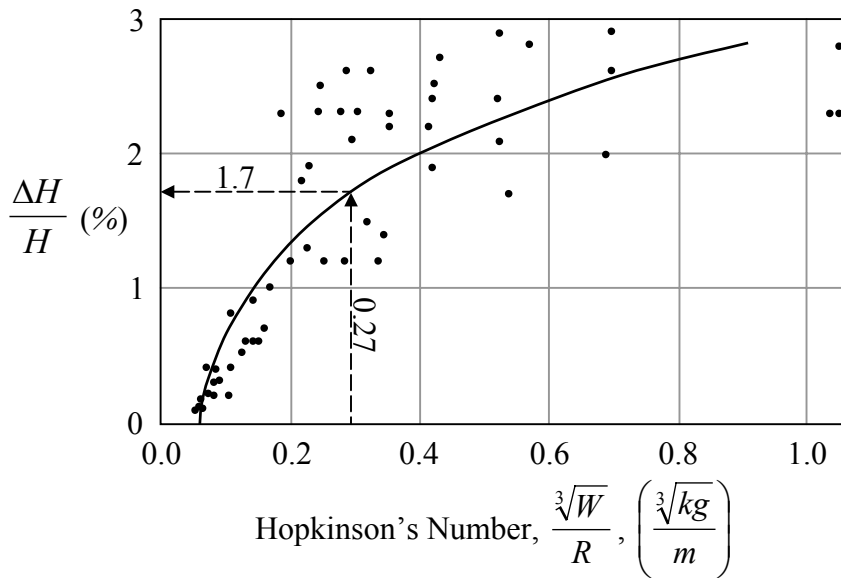
Figure 7-43. Correlation relating *HN* and surface settlement expressed in terms of vertical strain. (Adapted from Kok 1981).

An average fit of the data shown in Figure 7-43 is given by Equation (7-14).

$$
\frac{\Delta H}{H}(\%) =
\begin{cases}
0 & \text{for} \quad \dfrac{\Delta u_{sd}}{\sigma'} < 0.8 \\[3ex]
2.73 + 0.9 \cdot \ln\left(\dfrac{\sqrt[3]{W}}{R}\right) & \text{for} \quad \dfrac{\Delta u_{sd}}{\sigma'} \geq 0.8
\end{cases}
\qquad \text{(average)} \qquad (7\text{-}14)
$$

where: ΔH = Surface settlement as a result of blasting.

H = Initial thickness of loose deposit (same units as ΔH).

Δu_{sd} = Semi-dynamic pore pressure.

σ' = Original effective stress (same units as Δu_{sd}).

W = Weight of charge in equivalent *kg* of TNT (*kg*).

R = Distance from center of charge (*m*).

Using Equation (7-14) and Figure 7-42, the required *R-W* combination for a targeted densification may be selected. In practice, spacing of the charges typically ranges from 1 to 2 times *R* (Narin van Court and Mitchell 1994b).

Before moving on to the next approach for determining the *R-W* combination, attention is focused on the pore pressure ratio $\Delta u_{sd}/\sigma'$. Studer and Kok (1980) make the following statements about semi-dynamic pore pressure (Δu_{sd}): "When a transient loading is severe the grain structure of the sand may, under certain conditions, collapse and consolidation takes place. Porewater is squeezed out and this process is mainly governed by the permeability of the sand. The porewater pressure dissipates and is measured as a slowly proceeding phenomenon, taking place in a time range from several minutes to several days." If it is assumed that σ' (referred to as "the original effective stress" in Kok and Trense 1979) is the initial effective overburden (σ'_{vo}), then by all accounts $\Delta u_{sd}/\sigma'$ is the same as the residual excess pore pressure ratio (r_u) used in earthquake liquefaction studies.

However, if $\Delta u_{sd}/\sigma' = r_u$, it is uncertain why $\Delta u_{sd}/\sigma'$ reaches values well above 1.0, the upper limit of r_u. In this regard, Kok (1981) states: "For a specific site it is valid that

$\Delta u_{sd}/\sigma'$ can reach a value of approximately 1.7. This is due to the fact that the pore pressure measuring device is not able to discriminate actual excess porewater pressure and a 'heavy' liquid." The author is uncertain what this statement means and hypothesizes that the data showing $\Delta u_{sd}/\sigma' \geq 1.0$ (i.e., five points in Figure 7-41) resulted from pore pressure transducers becoming uncalibrated from the high intensity shock wave or result from some sort of residual increase in the total pressure from the blast generated gas bubbles.

To gain a better understanding of the relationship between $\Delta u_{sd}/\sigma'$ and r_u, the following simple comparison is made. Using Equation (7-13a), $HN = 0.27$ was computed for $\Delta u_{sd}/\sigma' = 0.8$. Using Figure 7-43 or Equation (7-14), $\Delta H/H = 1.7\%$ for $HN = 0.27$. From the correlation presented in Ishihara and Yoshimine (1992) relating observed settlements during earthquakes to the maximum induced shear strain, $\Delta H/H = \varepsilon_v = 1.7\%$ falls in the range denoted as initial liquefaction for $D_r = 40\%$, as shown in Figure 7-44. Although this comparison does not conclusively prove that $\Delta u_{sd}/\sigma' = r_u$, it supports the hypothesis that the two parameters are essentially the same.
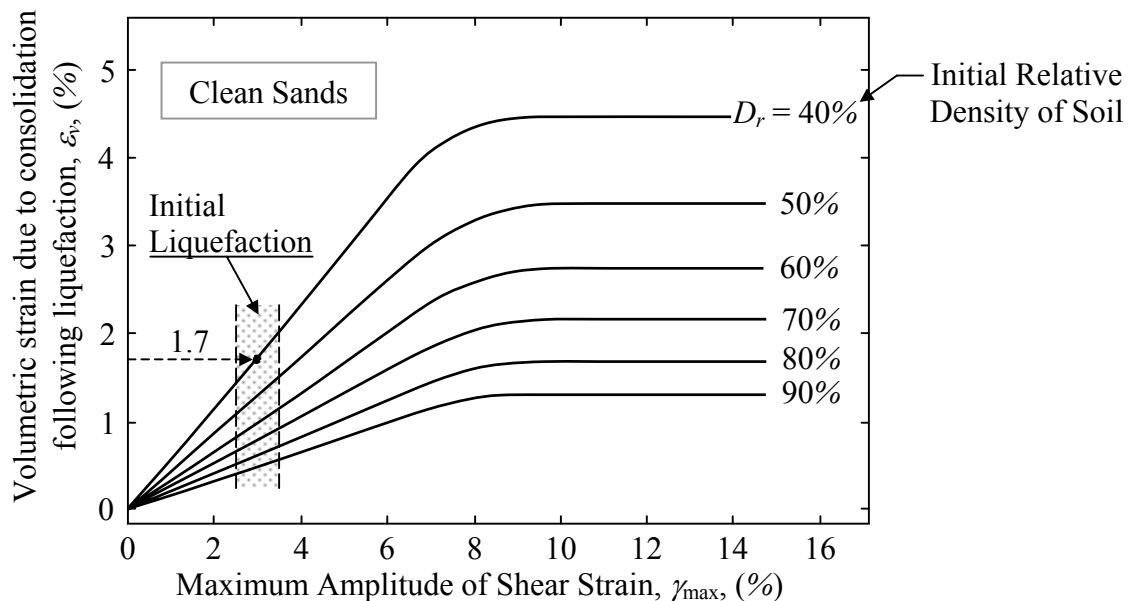

Figure 7-44. Comparison of the vertical strain corresponding to $\Delta u_{sd}/\sigma' = 0.8$ for blast data to the vertical strain from earthquake data. (Adapted from Ishihara and Yoshimine 1992).

7.4.2.2 Gohl et al. Approach

Gohl et al. (2000) outline a procedure relating the fraction of the maximum achievable vertical strain to charge weight. Starting with Equation 7-15a for vertical strain in a saturated soil and using the expression for relative density (Equation 7-15b), Gohl et al. (2000) derived an expression for the maximum achievable vertical strain, given as Equation 7-15c. In deriving this expression, Gohl et al. assumed that the maximum achievable relative density from blasting is 80%.

$$\varepsilon_v = \frac{\Delta e}{1+e} \tag{7-15a}$$

$$D_r = \frac{e_{max} - e}{e_{max} + e_{min}} \tag{7-15b}$$

$$\varepsilon_{v,max} = \frac{0.8 - D_{r,i}}{\dfrac{(1+e_{max})}{(e_{max}-e_{min})} - D_{r,i}} \tag{7-15c}$$

where: $\varepsilon_{v,\,max}$ = Maximum volumetric strain.

$D_{r,i}$ = Initial relative density.

e_{max} = Maximum void ratio.

e_{min} = Minimum void ratio.

e = Void ratio.

Δe = Change in void ratio.

D_r = Relative density.

For typical sand properties (e.g., $e_{max} = 1$ and $e_{min} = 0.5$), Equation (7-15c) can be approximated as:

$$\varepsilon_{v,max} \approx \frac{0.8 - D_r}{4 - D_r} \tag{7-15d}$$

The following empirical relation expresses the fraction of the maximum achievable volumetric strain, given by Equation (7-15d), to blast parameters (Gohl et al. 2000).

$$Eff = k \cdot \left(\frac{W}{\rho}\right)^{0.5} \frac{1}{h^{0.5}R} \qquad (7\text{-}16)$$

where:

Eff	=	The fraction of maximum achievable vertical strain.	
k	=	Site-specific attenuation factor.	
W	=	Weight of charge.	
ρ	=	Mass density of the explosive.	
R	=	The radius of a circle having an area equal to the tributary area of the charge.	
h	=	Depth of burial.	

Unfortunately, Gohl et al. (2000) do not specify the units of all the variables in Equation (7-16), a requirement for using empirical expressions. Several attempts were made to ascertain the units from the data presented in the paper but without success. Regardless, once Eff is determined from Equation (7-16), the volumetric strain resulting from blasting can be approximated as:

$$\varepsilon_v \approx Eff \cdot \varepsilon_{v,max} \qquad (7\text{-}17)$$

The vertical strains observed during several field densification programs are plotted as functions of the initial relative densities of the soil in Figure 7-45. Also shown in this figure are the maximum predicted strains determined from Equation (7-15d) and from the plateau of the curves shown in Figure 7-44. From this figure, it can be seen that settlements observed in the field range between those predicted using Ishihara and Yoshimine (1992) correlation and those computed using Equation (7-15d).
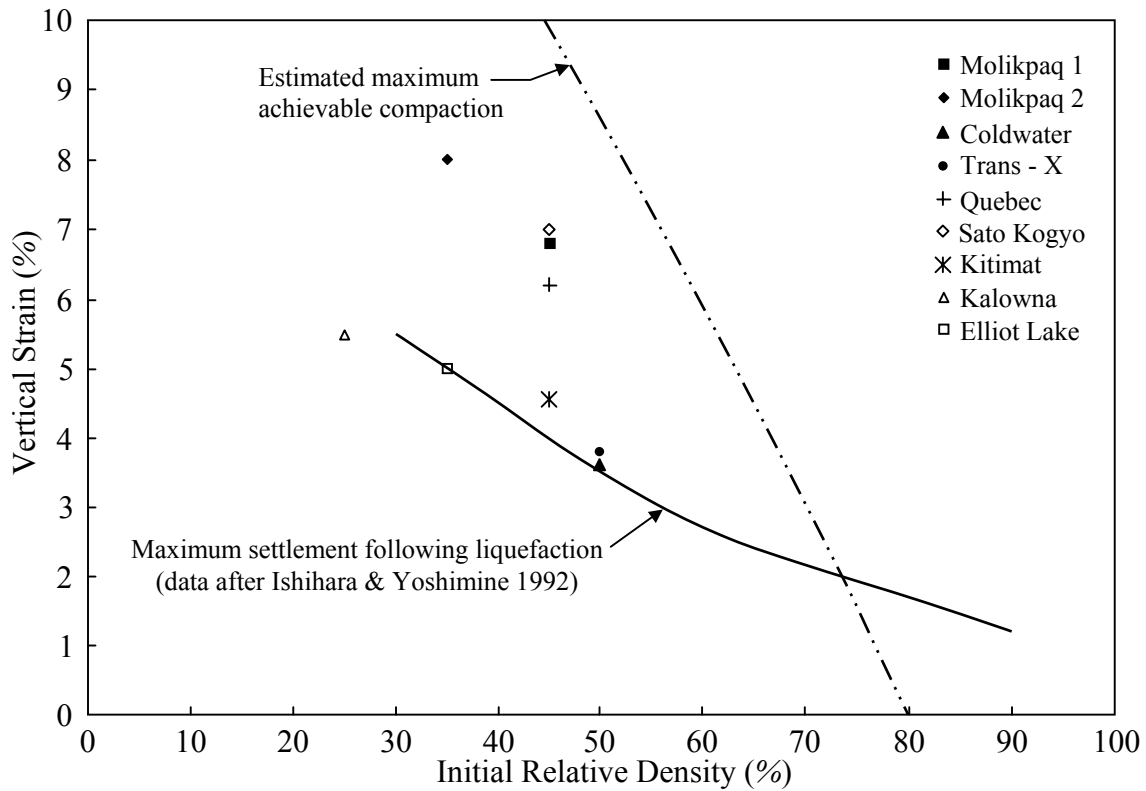
Figure 7-45. Comparison of observed strains to maximum values predicted by
Equation (7-15d) and from Figure 7-44. (Adapted from Gohl et al. 2000).

7.4.2.3 Narin van Court and Mitchell Approach

The final procedure reviewed is that proposed by Narin van Court and Mitchell (1998),
which expresses post-blast penetration resistance as a function of the initial penetration
resistance and blast parameters. The empirical expression developed by Narin van Court
and Mitchell (1998) is given as Equation (7-18).

$$q_{1,f} = 0.450 \cdot \left(\sum \frac{W_i}{R_i^2} \right)^{0.321} \cdot q_{1,o}^{0.5} \qquad (7\text{-}18)$$

where: $q_{1,f}$ =   Final normalized tip resistance in the given depth interval
                (*MPa*).

         W_i =   Weight of the individual charges surrounding the given
                interval (*grams*).

$$R_i \quad = \quad \text{Vector distance between the closest point of the individual}$$
charges and the middle of the given depth interval (*m*).

$$q_{1,o} \quad = \quad \text{Initial normalized tip resistance in the given depth interval}$$
(*MPa*).

In this expression, the normalized tip resistance is the average of a given depth interval, normalized to 1*ton/ft²* effective overburden pressure. It is assumed that q_{1f} corresponds to the normalized penetration resistance determined at a sufficient enough time after blasting that increases in the soil strength and stiffness have stabilized.

Comparisons of measured and predicted final normalized tip resistances for several field case histories are shown in Figure 7-46. The large amount of scatter in the data shown in this figure is testament to the complexity of explosive compaction and the influence of parameters such as site conditions.
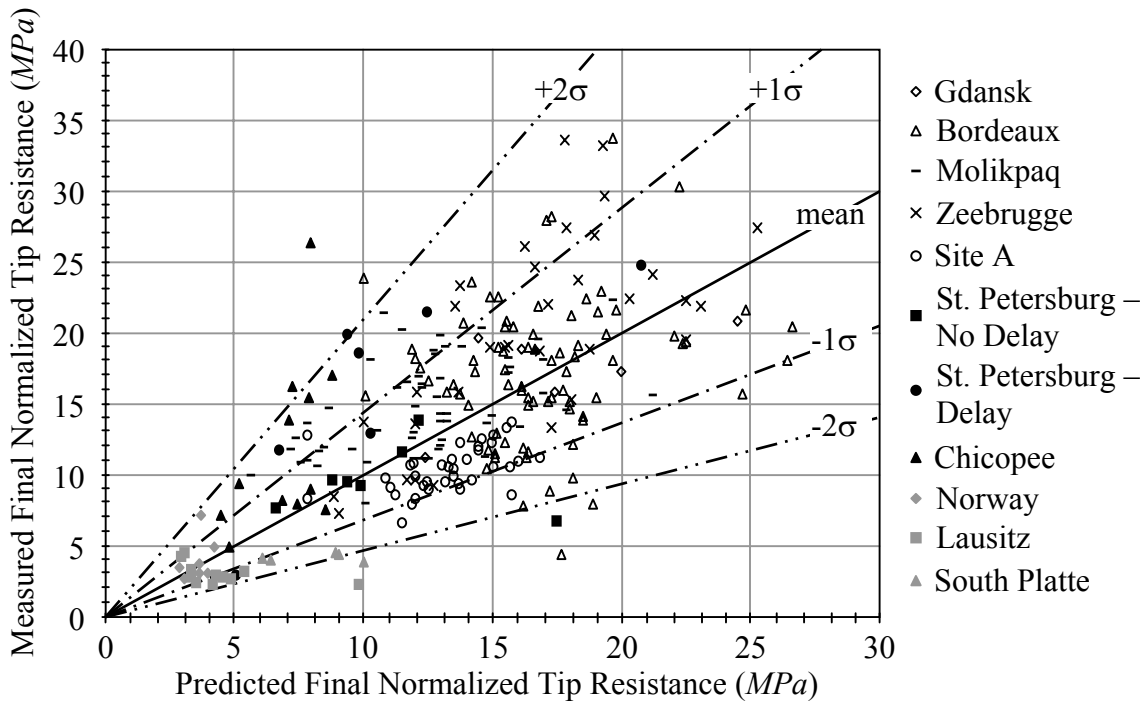

Figure 7-46. Comparison of measured and predicted final normalized tip resistances. (Adapted from Narin van Court and Mitchell 1998).

7.5 Comparison of the Mechanical Energy Input by the Densification Techniques

For comparison purposes, the following simple calculations are presented for estimating the mechanical energy required to densify a unit volume of soil using vibro-compaction, deep dynamic compaction, and explosive compaction. The term "Mechanical energy" refers to the energy that is available to do mechanical work, as opposed to energy expended in other forms (e.g., heat). The distinctions between the energies can be understood by considering deep dynamic compaction. The total energy expended during deep dynamic compaction could be quantified in terms of the fuel consumed by the crane that lifts the tamper. However, to avoid consideration of such things as the efficiency of the crane's combustion engine, the potential energy of the tamper at its drop height is used to approximate the (mechanical) energy per drop imparted to the soil. In the following analyses, the mechanical energies (per unit volume of soil) required to densify loose clean sand (Zone 1 soil, Figure 7-29) by vibrocompaction, deep dynamic compaction, and explosive compaction are computed and compared.

7.5.1 Vibro-Compaction

As described in Brown (1977) and D'Appolonia (1953), for electrically driven motors the current draw of the vibrator is used as an indicator of the compaction process: the current draw increases as the soil densifies. When the current draw "peaks," the vibroflot is raised to the next location, at which point, the current draw drops and compaction begins again. This process is illustrated in the current log shown in Figure 7-47 (Degen and Hussin 2001). As may be observed from this figure, the vibroflot rapidly penetrates the soil profile to the desired treatment depth of $8m$, with one up-down flushing of the machine after reaching $4m$. The penetration time was just over one minute. After reaching $8m$, the compaction process begins and is designated in this figure as $t = 0min$. The probe is raised in $0.5m$ intervals and held at each position for about $45sec$.

The average rate of work (i.e., power) performed on a soil by a vibroflot can be estimated as:

$$P = I \cdot E \cdot pf \cdot eff \cdot \frac{\sqrt{3}}{1000} \qquad \text{(e.g., Puchstein et al. 1954)} \qquad (7\text{-}19)$$

where: P = Average rate of work performed by vibroflot (i.e., power) (*kW*, *kJ/sec*).

I = Average line current (*Amps*).

E = Phase-to-phase voltage requirement of vibrator (*volts*).

pf = Average power factor (≈ 0.8).

eff = Efficiency of electric motor (i.e., portion of the electrical power consumed by the motor that is available to do mechanical work, ≈ 0.9).
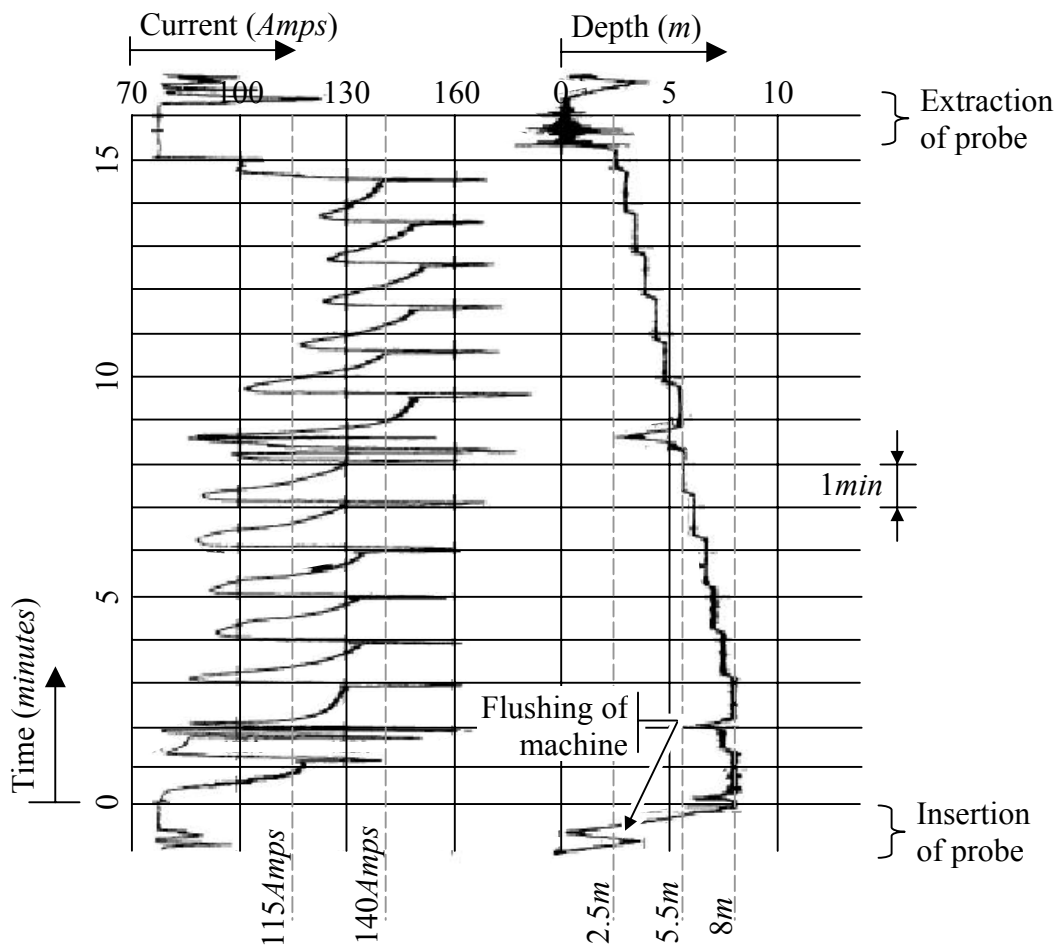

Figure 7-47. Current log recorded during vibrocompaction. (Adapted from Degen and Hussin 2001).

Based on the average current draw and the amplitude of the peaks, the profile may be considered as consisting of two layers: $2.5 - 5.5m$ and $5.5 - 8m$. The average current draws for the top and bottom layers are estimated to be about $140Amps$ and $115Amps$, respectively. For the Vibro V23 vibrator (i.e., $440volts$) and using Equation (7-19), the rates of work (P) performed by vibroflot on the top and bottom layers are estimated to be about 77 and $63kW$, respectively.

Knowing the compaction rate, the rate of work performed, and tributary area per compaction point, the mechanical energy required to treat a unit volume of soil can be determined. From Figure 7-47, the compaction rate is estimated to be about $0.37m/min$ (i.e., $(8m - 2.5m)/15min$; the probe was withdrawn from the ground at $2.5m$). This is in reasonable agreement with the typical rate of $0.3m/min$ given in Mitchell (1981). From Figure 7-10 the tributary area per compaction point is estimated to be about $80ft^2$ ($\approx 7.5m^2$). Finally, the range in the mechanical energy expended to treat a unit volume of soil in the profile corresponding to the current log shown in Figure 7-47 is:

$$\left(63 \, to \, 77kW\right) \cdot \left(\frac{\min}{0.37m} \cdot \frac{60\sec}{\min}\right) \cdot \frac{1}{7.5m^2} = 1362 \, to \, 1665kJ \, / \, m^3$$

7.5.2 Deep Dynamic Compaction

From Table 7-4, the mechanical energy required to densify Zone 1 soils ranges from 200 to $250kJ/m^3$.

7.5.3 Explosive Compaction

The quantity of explosive required to treat a unit volume of soil by deep explosive compaction is given in Van Impe and Madhav (1995) as ranging from 15 to $35g/m^3$. Similarly, from the case histories listed in Ivanov (1967), a range of 8 to $28g/m^3$ can be reasonably assumed. From calorimeter measurements, the energy density of TNT is approximately $4560J/g$. However, upon detonation, only about 67% of this energy is transformed into mechanical energy (Kennedy 1996). From the values stated above, the mechanical energy required to treat a unit volume of soil by explosive compaction is estimated to range from 22 to $100kJ/m^3$.

7.5.4 Discussion

In summary, the following ranges of mechanical energy per unit volume of treated soil are:

Vibro-Compaction:	1362 to 1665 kJ/m^3
Deep Dynamic Compaction:	200 to 250 kJ/m^3
Explosive Compaction:	22 to 100 kJ/m^3

From comparison of these ranges, explosive compaction appears to be the most efficient and vibrocompaction the least efficient (i.e., explosive compaction requires less mechanical energy to treat a unit volume of soil than the other techniques, etc.). The probable reason for the resulting efficiency rankings is the mode in which the energy is transferred to the soil by each of the remediation techniques. In vibrocompaction, the energy is imparted over a relatively long time span, during which the properties of the soil are continually changing. When liquefaction is induced in the soil immediately surrounding the probe, little energy is transferred from the probe to the outer, non-liquefied soil, during which time the majority of the imparted energy is expended inducing vibrations in the already liquefied soil. Furthermore, as may be recalled from Section 7.1, vibrocompaction improves the ground by both densifying the soil and increasing the lateral confining pressure. The latter improvement largely results from the lateral compaction of backfill. Accordingly, the energy range listed above reflects both the energy required to induce liquefaction in the virgin profile and the energy expended to laterally compact the backfill material.

For deep dynamic compaction, the energy is rapidly imparted to the soil. However, a large portion of the energy is likely carried by surface waves (Figure 7-35), which have little effect in breaking down the soil structure at depth in the profile. This is in contrast to deep explosive compaction, wherein the initial mechanical energy imparted to the soil is carried by body waves (primarily compression-extension waves), which are more effective in breaking down the soil structure than surface waves. Analogous to deep dynamic compaction is explosive compaction where the charge is placed at the surface of

303

the soil profile, as opposed to buried deep within the profile. From the case histories listed in Ivanov (1967), the quantity of explosives required to treat a unit volume of soil by surface blasting is approximately five to ten times greater than required for deep blasting, thus densification by surface blasting has an efficiency comparable to deep dynamic compaction.

As may be recalled from Chapter 5, the ability of the soil to resist liquefaction (i.e., *Capacity*) was quantified in terms of dissipated energy per unit volume, which is computed by integrating the stress-strain hysteresis loops up to initial liquefaction. From the *Capacity* curve derived from earthquake case histories (i.e., Equation (5-11) or Figure 5-11), the dissipated energy per unit volume required to induce liquefaction can be determined. For soils confined at an effective pressure of $100kPa$ and having $N_{1,60}$ from 5 to $15blws/ft$, the dissipated energy required to induce liquefaction ranges from 0.03 to $0.192kJ/m^3$. This range is several orders of magnitude less than the ranges listed above for the mechanical energy required to densify a unit volume of soil by vibrocompaction, deep dynamic compaction, or explosive compaction. Ultimately, all the mechanical energy imparted to the soil by the densification techniques "dissipates," but much of it by radiating away from the immediate zone being treated (i.e., radiation damping). Accordingly, proper use of the earthquake *Capacity* curve for remedial ground densification design requires knowledge of the spatial distribution of the dissipation of the mechanical energy imparted to the soil during remedial ground densification. In the next chapter, first order numerical models are proposed for computing such spatial distributions.

7.6 Summary

In this chapter, vibro-compaction, deep dynamic compaction, and explosive compaction techniques were reviewed. Discussions were presented on both the mechanisms associated with these techniques for breaking down the soil structure and the empirical design procedures for implementing the techniques. Finally, a comparison was made of the mechanical energy imparted to the soil by the densification techniques to treat a unit volume of soil. Although this comparison allowed the ranking of the relative energy

efficiencies of the remediation techniques, the calculations used to compute the imparted mechanical energies did not provide any information on the how the energy is spatially dissipated in the soil. Such information is needed if comparisons are to be made between the dissipated energy required to induce liquefaction during remedial ground densification and during earthquakes.

In the next chapter, first order numerical models are proposed for computing the spatial distribution of the energy dissipated in the soil during treatment. This information is used in conjunction with the energy-based *Capacity* curve to predict the spatial extent of induced liquefaction. Based on the hypothesis that liquefaction is a requisite for the densification of saturated sands, the predicted extent of liquefaction predicted using proposed numerical models are compared with the spatial extent of improvement predicted using the empirical expressions and guidelines presented in this chapter.